TÜBİTAK

Turkish Journal of Earth Sciences

http://journals.tubitak.gov.tr/earth/

Research Article

Turkish J Earth Sci
(2019) 28: 372-397

doi:10.3906/yer-1805-36

Zircon U-Pb geochronology, geochemistry, Sr-Nd isotopic compositions, and tectonomagmatic implications of Nay (NE Iran) postcollisional intrusives in the Sabzevar zone

Alireza ALMASI[1,2], Mohammad Hassan KARIMPOUR[2], Reza ARJMANDZADEH[3,*], Jose Fransisco SANTOS[4], Khosrow EBRAHIMI NASRABADI[2]

[1]Department of Geology, Faculty of Science, Lorestan University, Khorramabad, Iran
[2]Department of Geology, Ferdowsi University of Mashhad, Mashhad, Iran
[3]Department of Geology, Payame Noor University, Tehran, Iran
[4]Geobiotec, Department of Geosciences, University of Aveiro, Aveiro, Portugal

Received: 30.05.2018 • **Accepted/Published Online:** 10.02.2019 • **Final Version:** 10.05.2019

Abstract: The mafic to felsic intrusive rocks of Nay (IRN) are located in the northeast of the central Iranian block. In this study, we present new major and trace element geochemistry, U-Pb zircon ages, and Sr-Nd isotopic data to discuss the origin of the IRN postcollisional units. The oldest units in the Nay area belong to Paleocene–early Eocene volcanic and pyroclastic series including basalt-andesite, latite, dacite, and tuff. These series are crosscut by subvolcanic and granitoid rocks with lithological composition varying from quartz gabbro to K-feldspar granite. The youngest igneous activity is represented by quartz monzodiorite dikes. Hornblende-biotite quartz monzonite from Nay granitoids was dated at 40 Ma (zircon U-Pb). The IRN rocks are metaluminous to peraluminous with high-K calc-alkaline and shoshonitic affinities. They display enrichment in light REEs [$(La/Yb)_N$ = 3.79–8.71] and LILEs (such as Ba, Th, Rb, U, and K), with depletion in HFSEs (such as Nb, Zr, Y, and Ti). All rocks have negative Eu anomalies [$(Eu/Eu^*)_N$ = 0.17–0.88] and relatively flat heavy REE patterns [$(Gd/Yb)_N$ = 1.12–1.69]. Granitoids have initial $^{87}Sr/^{86}Sr$ values from 0.7053 to 0.7061 and εNd values from –1.65 to –0.02 calculated at 40 Ma. The geochemical composition of IRN rocks along with the low I_{Sr} and positive εNd values and mantle model ages of 0.6–0.8 Ga indicate that two end-members, enriched mantle and a continental crust, were involved in the magma generation. We argue that the Eocene IRN magmatism occurred as a postcollisional product by asthenospheric upwelling owing to the convective removal of the lithosphere during an extensional collapse of the central Iranian block.

Key words: Nay intrusive rocks, postcollisional, Sr-Nd isotopes, zircon U-Pb dating, asthenospheric upwelling, Sabzevar oceanic crust

1. Introduction

Calc-alkaline I-type plutonic rocks, which include subduction-related and collisional magmatic suites, are common in many different convergent tectonic settings. Genetic classification of such plutonic rocks is based on the amount of crustal, mantle, or mixed components involved during their generation (Barbarin and Didier, 1992; Chappell and White, 1992; Sisson and Grove, 1993; Altherr et al., 2000; Chen et al., 2002).

Iran and the surrounding areas consist of a mosaic of continental blocks (Tethyan blocks), including the Pontides, Anatolide–Taurides, Afghanistan, Songpan–Ganzi, Eastern Qiangtang, Western Qiangtang, Lhasa, Indochina, Sibumasu, and Western Burma blocks, delimited by complex fold-and-thrust belts within the Alpine-Himalayan orogenic system (Gansser, 1981; Şengör and Yilmaz, 1981; Şengör, 1990). Apart from Gondwana during the Tethyside orogenic system, they drifted northwards, then joined the Eurasian continent by the opening and closing of two successive and partly contemporaneous Tethyan oceanic basins (the older northern Paleo-Tethyan and the younger southern Neo-Tethyan), followed by continental collision (cf. Stampfli and Kozur, 2006).

The tectonic episodes of Iran have been influenced by the opening and closure of the Paleotethys in the Paleozoic and the closure of the Neotethys in the Cenozoic. The closure of the Paleotethys resulted in the separation of the Cimmerian terrain from the Gondwanan passive margin and the opening of the Neo-Tethyan Ocean (Allegre et al., 1984; Stampfli and Borel, 2002). The Neo-Tethys constitutes several oceanic remains (ophiolites and

* Correspondence: r.arjmandzadeh@pnu.ac.ir

mélanges) along some Mesozoic sutures, which include the Zagros suture in Iran and the Bitlis suture in Turkey (Şengör, 1987; Şengör and Natalin, 1996).

After the Paleo-Tethyan Ocean was closed, the Neo-Tethys began to subduct under the Cimmerian plate that was newly joined to the Eurasian continent. Some Jurassic–Cretaceous arc settings formed along the south of Eurasia, including the Pontides back-arc setting in northeastern Sakarya (Kaygusuz et al., 2008; Karsli et al., 2010; Kaygusuz, 2011), the Sabzevar back-arc basin (Baroz et al., 1984; Shafaii Moghadam et al., 2014) (Figure 1), and the Sanandaj–Sirjan arc in central Iran (Shahabpour, 2005). At the end of the Cretaceous, when the Neo-Tethys closed (Stöcklin, 1968; Berberian and King, 1981; Şengör, 1987; Alavi, 1996, 2007; Şengör and Natalin, 1996; Dilek et al., 2007), these magmatic arcs were joined to the south of the Eurasian plate (Golonka and Bocharova, 2000; Shahabpour, 2005).

The closure of the Neo-Tethys and collision of the Arabian and Eurasian continents during the late Eocene-Oligocene (Koop et al., 1982; Vincent et al., 2005; Allen and Armstrong, 2008; Agard et al., 2011; Ballato et al., 2011; Mouthereau et al., 2012) resulted in the formation of the Iranian–Turkish Plateau. The continuation of the collision resulted in crustal thickening and the extension of the associated thrusting (Ramsey et al., 2008), followed by normal faulting, extensional tectonic settings, magmatic flare-up, and exhumations of metamorphic core complexes (Verdel et al., 2011; Shafaii Moghadam et al., 2016) (Figure 1).

An important magmatic flare-up occurred in Iran and Turkey in the Eocene-Miocene period, which lead to the formation of a calc-alkaline or high-K calc-alkaline volcanic plutonic belt (Pearce et al., 1990; Verdel et al., 2011). The Urumieh-Dokhtar magmatic arc/belt (UDMA) is the most important Eocene-Miocene magmatic episode in Iran (Omrani et al., 2008; Ahmadian et al., 2009; Shafiei et al., 2009; Aghazadeh et al., 2010; Verdel et al., 2011; Chiu et al., 2013) (Figure 1). Some of the other outstanding Eocene magmatic zones in Iran include the Alborz magmatic arc (Aghazadeh et al., 2010; Asiabanha and Foden, 2012), Sabzevar magmatic zone (Verdel et al., 2011; Alaminia et al., 2013; Chiu et al., 2013), Lut-Sistan zone (eastern Iranian suture zone) (Arjmandzadeh et al., 2011, Pang et al., 2013; Arjmandzadeh and Santos, 2014), and Khaf-Kashmar-Bardaskan volcano-plutonic belt (KKBB; north of Lut block; Figure 1) (Karimpour, 2004; Malekzadeh Shafaroudi et al., 2013; Shafaii Moghadam et al., 2015).

Several recent models proposed for the dominant Eocene magmatism in Iran and Turkey include: 1) postcollisional slab breakoff (Boztuğ et al., 2007; Keskin et al., 2008; Omrani et al., 2008; Aghazadeh et al., 2010; Dilek et al., 2010; Malekzadeh Shafaroudi et al., 2013; Shafaii Moghadam et al., 2015); 2) postcollisional crustal thickening (Topuz et al., 2005; Shafiei et al., 2009; Verdel et al., 2011) and delamination of the thickened crust (Dilek et al., 2010; Karsli et al., 2010; Arslan et al., 2013; Aslan et al., 2014), and 3) slab window-related processes (Shafiei et al., 2009; Eyuboğlu et al., 2011).

Prior to this study, numerous geochemical and petrological investigations have been conducted on various intrusive bodies of the KKBB belt (Soltani, 2000; Malekzadeh Shafaroudi et al., 2013; Shafaii Moghadam et al., 2015). The present study focuses on the mafic to felsic intrusive rocks of Nay (IRN) in the KKBB belt, the least-studied ones among other plutonic rocks in the KKBB belt. We present new whole-rock geochemical data of mafic to felsic rocks and Sr-Nd isotopic data as well as U-Pb zircon ages of granitoids and determine their magma sources and evolution. Furthermore, this dataset helps achieve a comprehensive understanding of the magmatic and tectonic evolution from the Eocene to Oligocene in the Alborz-Sabzevar and Lut-Sistan zone.

2. Geology

The study area is located in the center of the Tertiary metallogenic volcano-plutonic belt of the KKBB (Karimpour, 2004) (Figure 1). This belt is located between the old Dorouneh and Taknar faults in the south and north of the study area, respectively (Figure 1). Tectonic studies on the faults of the NE and E of Iran (Walker and Jackson, 2004) confirm that the Dorouneh and Taknar faults had sinistral strike-slip movement in at least 5–7 Ma of the late Cenozoic, but plate tectonic reconstructions attest that the overall movements have been uniform since ~56 Ma (McQuarrie et al., 2003). The oldest rocks in the KKBB belong to the Taknar inlier near the east of the city of Kashmar. The Taknar inlier is a segment of Central Iranian Precambrian-Paleozoic continental crust basement (zircon U-Pb dating on Bornaward granitoids, 540–550 Ma, late-Neoproterozoic; Bagherzadeh et al., 2015), which uplifted during the Eocene continental collision between the Arabian and Eurasian continents.

The geology of the KKBB mainly includes Cenozoic felsic to mafic volcanic rocks (Figure 1), which have been intruded by granitoid rocks of granitic to dioritic composition (Eftekharnezhad et al., 1974; Afsharharb et al., 1987; Sahandi and Hoseini, 1990; Vaezipour et al., 1993; Naderi Mighan and Torshizian, 1999). The only isotopic age for the host volcanic rocks in the KKBB has been reported by Bernhardt (1983), giving ages of 57.2 ± 3.7 Ma and 43.7 ± 1.7 Ma using K-Ar dates on hornblende and biotite, respectively. Since the hornblende is more highly retentive with respect to ^{40}Ar than biotite (Faure, 1986; McDougall and Harrison, 1988), the obtained age is

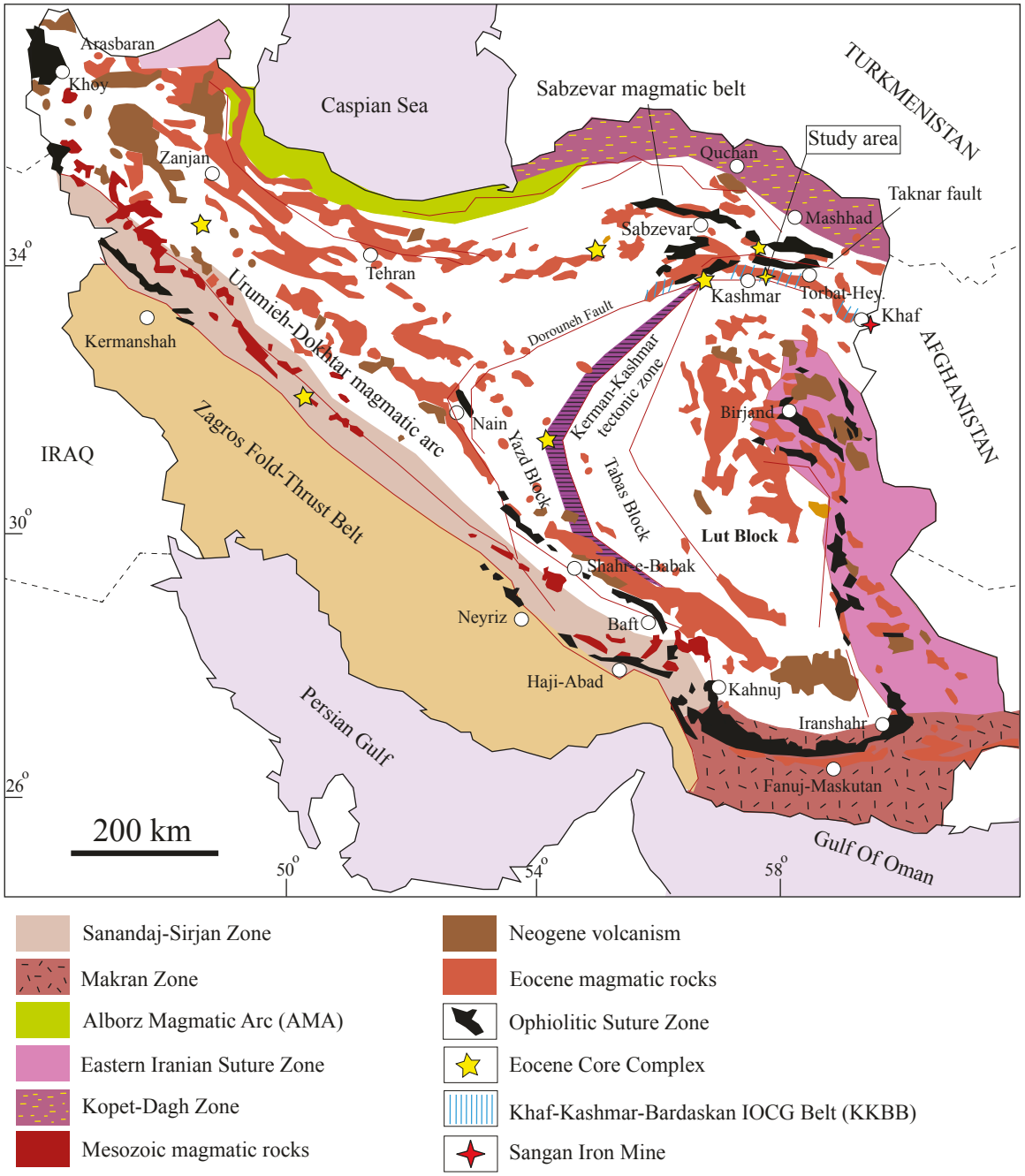

Figure 1. Simplified geological map of Iran showing the distribution of Eocene magmatic rocks (modified after Shafaii Moghadam et al., 2015). The distribution of core complexes is according to Verdel et al. (2007) and Alaminia et al. (2013).

interpreted as the emplacement age of the volcanic rocks, whereas the younger age for biotite may be the result of ^{40}Ar resetting due to the replacement and influence of granitoids with similar ages (Soltani, 2000).

Based on the geological map of Feyzabad (scale 1:100,000) (Behroozi, 1987), the granitoids intruded subaerial Paleocene–Eocene pyroclastic and Early to Middle Eocene mafic to felsic volcanic rocks (Behroozi, 1987). Previous studies on the Kashmar and Sangan granitoids (Soltani, 2000; Malekzadeh Shafaroudi et al., 2013; Shafaii Moghadam et al., 2015) indicate that these rocks are high-K calc-alkaline in composition and I-type and emplaced during Eocene time (Zircon U-Pb dating; Shafaii Moghadam et al., 2015).

A new detailed geological map is presented here for the Nay area (Figure 2). Field relationships indicate the

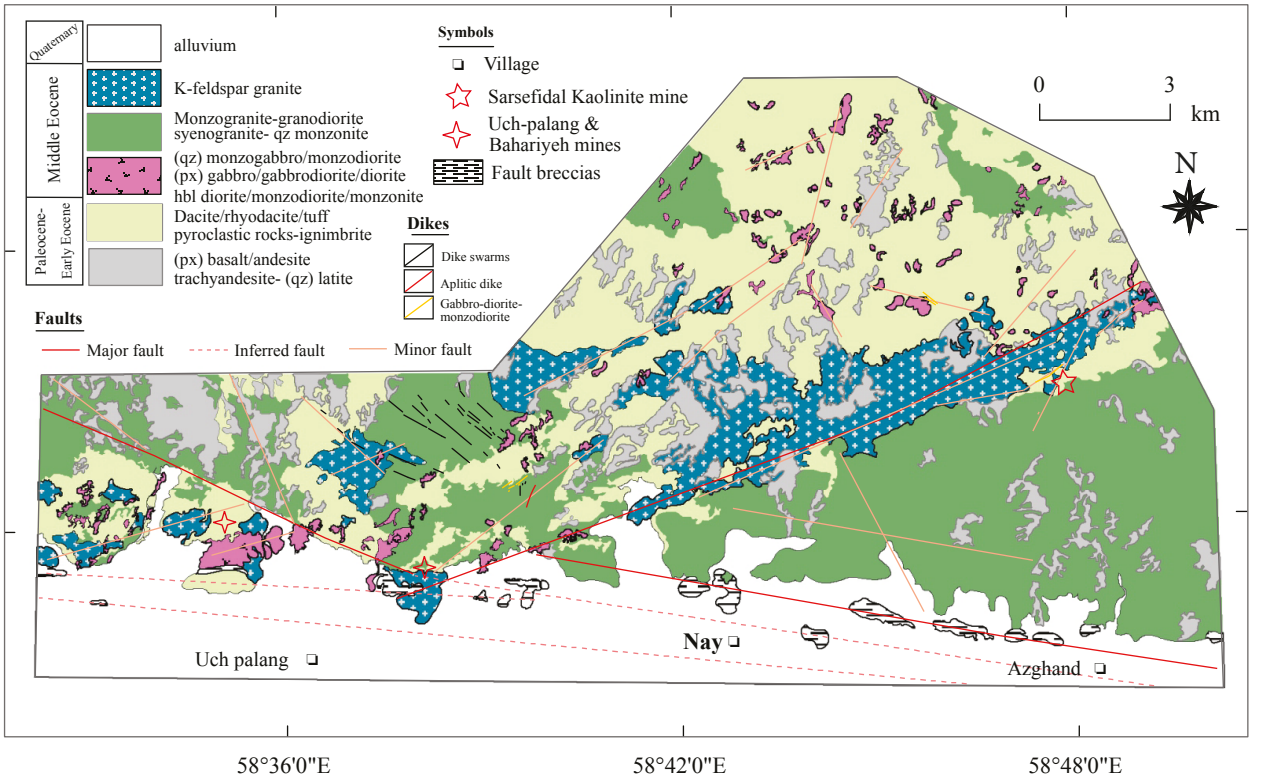

Figure 2. Geological map of the Nay working area.

following sequence of magmatic events in the area (Figure 2): 1) Old mafic volcanic series including (pyroxene) basalt/andesite and minor trachyandesite and (quartz) latite. These rocks occupy the north and northeast of the village of Nay (Figure 3A). Propylitic alteration (chlorite, epidote, and calcite) affected these rocks. 2) Old felsic volcanic series such as dacite, rhyodacite, tuff (lapilli tuff, sandy tuff, layered tuff, and crystal lithic tuff), pyroclastic rocks and ignimbrite, and minor rhyolite (Figure 3B) are widespread in the study area. As mentioned above, Bernhardt (1983) gives a Paleocene age for these rocks. These units are intensely subjected to argillic, sericitic, and silicified alterations, especially in crosscutting points of faults. 3) Subvolcanic bodies including (quartz) monzogabbro/monzodiorite, pyroxene gabbro/gabbrodiorite/diorite, and hornblende diorite/monzodiorite/monzonite. The mafic volcanic units are intruded by these intrusive bodies (small stocks and dikes) and usually altered to chlorite and epidote. 4) Granitoids have composition ranging from granodiorite and monzogranite to syenogranite and k-feldspar granite as well as minor amounts of quartz monzonite and monzonite with aplitic dikes. They crop out especially in the north of Nay and Uch Palang villages and intruded into the felsic volcanic suites from eastern to western termination (Figures 3A–3C). Mafic microgranular enclaves (in clot forms and/or hornblende clusters) of different sizes and types and greenish color are commonly observed within the granitoids (Figure 3D). 5) Dike swarms (quartz monzodiorite porphyry) crosscut the volcanic rocks and granitoids in a NW-SE trend (Figure 2).

The IRN bodies have commonly been affected by late magmatic processes and hydrothermal episodes, such as sericitization, argillation, carbonatization, chloritization, and tourmalinization, especially along the faults and veins. Except for dike swarms, all rocks experienced alterations. New alteration and mineralization studies (Almasi, 2016) indicate the occurrence of iron oxide copper-gold (IOCG, Figure 1) mineralization in the Nay area.

3. Petrography of subvolcanic and plutonic rocks

3.1. Subvolcanic rocks

The intermediate to mafic subvolcanic intrusives consist of quartz diorite, quartz monzodiorite, monzogabbro, monzonite, and quartz gabbro with an exposed surface area of approximately 200 m^2 to 2 km^2. Since some samples from this group have distinct geochemical and petrographic features that separate them from other subvolcanic rocks, the group is subdivided into two classes.

Quartz gabbro and quartz monzodiorite crop out as several small stocks in the area. These intrusives with intergranular texture have a modal amount of minerals, including 3%–13% quartz up to 0.2 mm long, 30%–40%

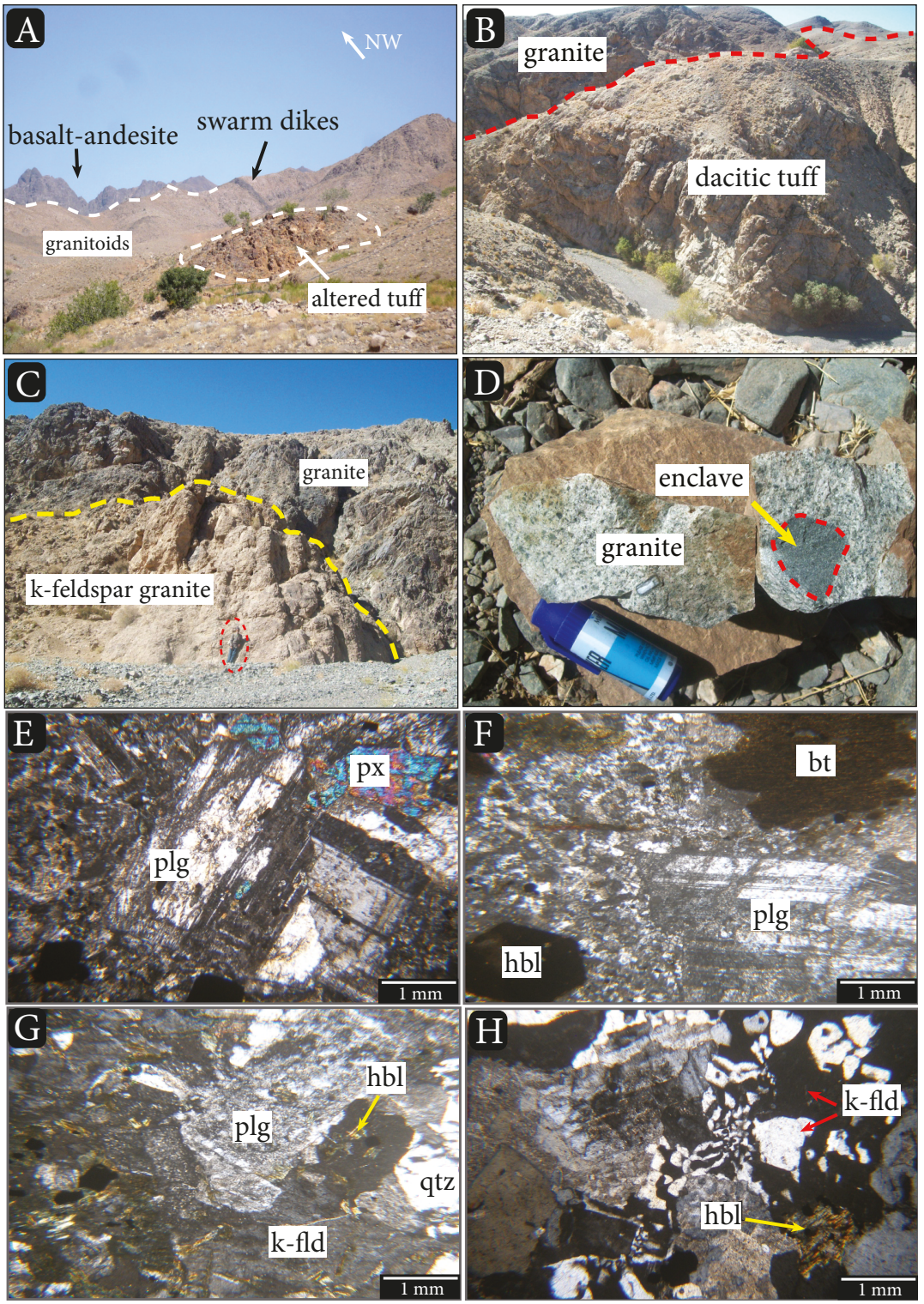

Figure 3. (A–D) Field photos of IRN bodies. (A–C) Granitoids intruded into volcanics and dike swarms cut older rocks including volcanics and granitoids. (D) Dioritic enclaves in granodiorite. (E–H) Micrographic photos of IRN bodies. (E) Clinopyroxene and plagioclase assemblages in the px gabbro (sample SP-20). (F) Association of plagioclase, biotite, and hornblende in biotite hornblende quartz monzonite/monzodiorite (BP-11). (G) Quartz, K-feldspar, plagioclase, and hornblende in hbl granite (SP-7). (H) Myrmekitic texture in K-feldspar granite (SP-18). plg: Plagioclase, px: pyroxene, hbl: hornblende, bt: biotite, k-fld: k-feldspar, qz: quartz.

plagioclase laths up to >1 mm, 5%–35% K-feldspar up to 0.5 mm, and <15% pyroxene (probably orthopyroxene). Other rocks of this group, including gabbrodiorite, quartz diorite, monzodiorite, and monzonite, have mineral assemblages including plagioclase, clinopyroxene (augite), hornblende, biotite, and quartz with accessory minerals including apatite, magnetite, and titanite (Figure 3E). These rock series display intergranular, porphyritic, ophitic, and glomeroporphyritic textures.

3.2. Granitoids

Nay granitoids consist of mainly monzogranite, granodiorites, syenogranite, and K-feldspar granite, along with minor quartz monzonite (Figures 2, 3F, and 3G). Quartz, plagioclase, alkali feldspar, and biotite, along with minor clinopyroxene and amphibole, are the dominant phases. Accessory phases include apatite, zircon, and iron oxides. Anhedral grains of quartz are clustered between plagioclase and orthoclase and make granophyric, micrographic, and myrmekitic intergrowths (Figures 3G and 3H). These rocks display granular, graphic, myrmekitic, and perthitic textures (Figures 3F and 3G). Microgranular enclaves occur (Figure 3D), and they are especially abundant in the northeast of the area. Enclaves have compositions ranging from granodiorite to diorite, which dominantly are granodioritic with small crystals of amphibole and plagioclase. Dioritic enclaves containing plagioclase, orthopyroxene, and clinopyroxene also prevail.

Granodiorites are abundant rock units and contain quartz, K-feldspar orthoclase and microcline, plagioclase, amphibole, biotite, and rarely clinopyroxene. Coarse-grained plagioclase crystals range in size from 2 to 4 mm and are partially replaced by sericite during alteration. Minor phases include iron oxides, apatite, zircon, and titanite.

The mineralogical assemblage of quartz monzonite intrusives is similar to that of monzogranites but with more plagioclase. Various mafic, intermediate, and felsic dikes exist in the Nay area (Figure 2). Felsic dikes intruded into granitoids and their host volcanic edifices, indicating a close genetic relationship. Cataclastic veins containing tourmaline are also common in granitoid rocks.

3.3. K-feldspar granite

This granite shows petrographic characteristics as an end-member of the granitoid suite. All samples have a light pink color in hand specimens and lack ferromagnesian and opaque minerals in transmitted light examination (rarely fine grain biotite and hornblende and magnetite). The mineral assemblage is coarse to moderately grained. Mineralogy comprises a simple and modal amount of minerals including 20%–25% quartz up to 2.5 mm, 30%–45% K-feldspar (orthoclase, perthite, and microcline) of 1–2.5 mm, 20%–30% albite, and oligoclase of 1–2 mm.

Accessory minerals include magnetite, zircon, and apatite. K-feldspar usually occurs as microperthitic intergrowths. Microperthite commonly displays string, vein, and braid varieties. Microcline is recognized by typical development of cross-hatched twinning characteristic of combined albite and pericline twins, indicating low-temperature feldspar. Orthoclase is widespread and typically displays Carlsbad twinning. It varies from 1 mm to 6 cm in length and occurs generally as turbid, euhedral, and tabular megacrysts.

3.4. Dike swarms

These rocks have mineralogy and texture similar to subvolcanic rocks. The mineral assemblage of plagioclase, quartz, K-feldspar, hornblende, clinopyroxene, apatite, and magnetite indicates quartz monzodiorite in composition. The mineral content indicates that the mafic dikes were influenced by retrograde reactions and reequilibrated during the fall in temperature. These features are supported by uralitization and saussuritization of pyroxenes and plagioclases respectively due to the autometamorphism attributed to the action of the exsolved volatiles (Li, 2013).

4. Analytical techniques

4.1. Whole-rock geochemistry

This research is mainly founded on field reconnaissance, reflected and transmitted light microscopy, whole-rock elemental and isotopic geochemistry, and geochronology. After obtaining precise and detailed petrography of a larger set of rocks, 28 representative samples were selected for whole-rock analysis. The samples were powdered to <200 mesh by an agate mill, and the pulps were analyzed for major oxides and minor and trace elements using ICP-AES and ICP-MS, respectively, at ACME Laboratories (Vancouver, Canada). The accuracy and precision, as represented by the United States Geological Survey standards and duplicates, are within 1% for major oxides and 10% for trace elements. The major oxide and minor and trace element data for the IRN bodies are listed in Table 1.

4.2. Zircon U-Pb dating

After separating zircon grains by crushing, hydrofracturing, and handpicking, about 70 crystals from each sample were examined by scanning electron microscopy (SEM) for morphological investigations. The grains were cast in epoxy and polished, then imaged by cathodoluminescence (CL) with a FET Philips XL 30 electron microscope (15 kV and 1 nA) at the University of Silesia, Sosnowiec, Poland.

Zircon $^{206}Pb/^{238}U$ and $^{207}Pb/^{206}Pb$ ages were defined using a 193-nm solid-state Nd-YAG laser (NewWave UP193-SS) coupled to a multicollector ICP-MS (Nu Instruments HR) at the University of Vienna (Table 2). The analytical procedures are identical to those explained

Table 1. Chemical compositions of representative rock samples of the IRN bodies.

Sample	Subvolcanic bodies										
	BP-104	BP-25	BP-14	KP-101	BP-24	BP-28	KP-22	KP-33	BP-4	SP-20	KP-104
	1	1	1	2	2	2	2	2	3	3	3
(wt.%)											
SiO_2	52.65	50.81	54.34	59.17	58.86	57.52	62.06	56.86	61.08	62.33	63.68
TiO_2	0.98	1.41	0.84	0.64	0.81	0.86	0.81	0.77	0.85	0.81	0.62
Al_2O_3	12.8	12.78	13.05	15.15	14.14	15.10	15.09	14.11	14.85	15.36	14.92
Fe_2O_3	1.39	1.50	0.64	0.60	0.79	0.79	0.61	.068	0.77	0.50	0.50
FeO	11.25	12.21	5.19	4.86	6.38	6.40	4.98	5.52	6.26	4.85	4.05
MnO	0.32	0.54	0.12	0.16	0.18	0.21	0.14	0.18	0.15	0.13	0.13
MgO	6.44	11.1	4.19	4.55	3.99	4.54	3.37	4.92	3.22	2.83	3.15
CaO	0.61	0.56	0.66	4.04	5.14	5.68	3.92	4.88	3.21	4.80	2.49
Na_2O	2.62	2.12	1.86	3.45	3.46	2.93	3.55	3.97	4.91	3.45	4.68
K_2O	0.54	0.92	5.10	3.38	2.84	3.07	2.99	3.64	1.68	2.78	3.65
P_2O_5	0.29	0.26	0.19	0.26	0.21	0.50	0.39	0.30	0.36	0.33	0.28
LOI	4.76	4.11	5.11	3.03	2.05	1.47	1.34	3.39	1.78	1.07	1.23
Total	94.65	98.32	91.29	99.29	99.12	99.07	99.25	99.22	99.12	99.24	99.38
A/CNK	2.13	2.32	1.33	0.91	1.06	0.82	0.93	0.73	0.94	0.88	0.92
(ppm)											
Ba	81	279	983	535	465	760	532	670	598	556	707
Be	2	<1	2	1	1	<1	3	<1	1	4	<1
Rb	12	17	102	74	50	60	71	74	31	74	71
Sr	56	58	150	377	381	514	404	281	335	379	259
Ga	17	18	15	17	16	18	16	17	16	16	16
Ta	0.8	0.4	0.5	0.5	0.7	0.7	0.8	0.5	0.7	0.8	0.8
Th	8.6	4.8	6.5	7.4	7.1	7.5	8.4	8	7.7	7.8	9.9
U	3.2	1.3	1.4	2.1	2.2	1.9	2.2	2	1.6	1.9	2.4
Zr	189	134	175	204	175	183	237	217	206	235	243
Hf	6	4	4	5	5	4	5	5	5	6	6
Y	21	23	23	28	25	27	30	26	30	33	31
Cs	1	1	1	11	1	8	4	1	1	2	1
Nb	11	8	9	10	11	10	13	10	10	13	12
Co	20	24	20	10	15	19	9	13	12	10	5
V	146	243	144	126	148	211	117	177	120	116	93
La	12.1	20.2	14.8	24	24.5	23.5	27.9	24.3	25.8	27.3	26.3
Ce	32.9	43.1	33.8	48.9	50	51.6	56.5	50.5	53.7	58.7	57.2
Pr	3.76	5.21	4.22	6.40	5.94	6.19	6.70	6.30	6.38	6.99	7.17
Nd	15.7	22.4	18.3	19.5	24.5	29	27.8	28.3	28.2	29.8	25.3
Sm	3.50	4.70	3.76	4.76	5.03	5.10	5.76	5.15	5.92	5.70	6.03
Eu	0.5	1.09	0.84	1.22	1.29	1.39	1.35	1.29	1.40	1.37	1.29
Gd	3.25	4.79	3.73	5.39	5.60	5.38	5.47	5.65	5.88	5.77	5.24
Tb	0.51	0.66	0.57	0.74	0.80	0.70	0.77	0.73	0.80	0.79	0.79
Dy	3.40	4.12	4.23	4.45	4.91	4.35	4.82	4.64	4.73	5.31	4.30

Table 1. (Continued).

Ho	0.69	0.81	0.86	0.92	0.99	0.87	0.97	0.90	1.09	1	0.96
Er	1.88	2.41	2.23	2.79	2.76	2.39	3.01	2.62	2.67	3.08	3.14
Tm	0.35	0.35	0.38	0.43	0.44	0.37	0.45	0.44	0.40	0.47	0.45
Yb	2.35	2.32	2.63	2.78	2.80	2.68	2.81	2.75	3.06	2.76	3.09
Lu	0.35	0.38	0.36	0.41	0.45	0.37	0.48	0.44	0.47	0.47	0.52
(La/Yb)n	6.69	5.96	5.68	6.01	5.90	5.91	6.69	5.96	5.68	6.67	6.67
Eu/Eu*	0.45	0.70	0.69	0.74	0.74	0.81	0.74	0.73	0.73	0.73	0.70
∑REEs	81.2	112.5	90.7	123.5	130	133.9	144.8	134	140.5	149.5	141.8

Table 1. (Continued).

Sample	Subvolcanic bodies									
	KP-24	KP-60	KP-57	KP-41	BP-11	BP-102	KP-102	BP-103	R15907*	R15924*
	[3]	[3]	[3]	[3]	[3]	[4]	[5]	[2]	[6]	[6]
(wt.%)										
SiO_2	61.23	65.98	60.61	61.53	65.92	67.21	61.83	62.28	59.01	54.35
TiO_2	0.64	0.60	0.77	0.63	0.54	0.57	0.69	0.73	0.81	0.80
Al_2O_3	14.85	14.98	15.08	16.31	14.36	14.43	14.65	14.27	16.04	16.80
Fe_2O_3	0.50	0.45	0.66	0.50	0.52	0.49	0.57	0.59	0.76	0.95
FeO	4.05	3.60	5.35	4.09	4.24	3.97	4.61	4.74	6.18	7.70
MnO	0.42	0.09	0.12	0.18	0.11	0.12	0.14	0.13	0.10	0.10
MgO	3.24	2.01	3.91	1.10	2.62	1.95	3.12	3.01	2.76	4.27
CaO	1.93	2.09	4.61	1.42	2.73	0.46	3.45	3.51	4.26	4.18
Na_2O	4.23	4.04	2.97	2.20	3.18	3.72	4.17	3.86	4.15	4.81
K_2O	4.07	3.90	3.47	8.18	3.84	4.88	3.72	3.78	2.87	2.04
P_2O_5	0.54	0.20	0.27	0.27	0.17	0.20	0.38	0.28	0.21	0.20
LOI	2.25	1.48	1.42	2.96	1.12	1.38	1.96	2.12	1.62	2.60
Total	97.95	99.42	99.24	99.37	99.36	99.38	99.29	99.29	99.65	99.80
A/CNK	1	0.94	0.89	1.08	1.10	0.97	0.85	0.88	0.99	1.09
Ba	808	662	545	991	547	1475	701	723	505	295
(ppm)										
Be	<1	3	1	<1	4	1	3	1		
Rb	109	77	73	173	94	80	87	65	55	72
Sr	191	347	331	115	393	129	354	359	363	315
Ga	16	16	15	14	14	14	16	15	18	19
Ta	0.7	0.9	0.6	0.9	0.7	0.9	0.9	0.8		
Th	9.5	12.1	9.2	9.7	13.5	11.2	11.2	8.8	11	3
U	2.5	2.9	2.1	2	3.6	3.3	2.3	2.6	2	2
Zr	201	232	229	218	167	223	251	215	144	84
Hf	5	6	5	6	5	7	6	6		
Y	24	31	28	25	19	28	31	29	33	20
Cs	3	2	4	3	3	1	4	1		
Nb	11	14	12	11	8	13	15	12	8	4

Table 1. (Continued).

Co	7	7	14	5	10	4	11	10		
V	86	73	144	87	106	57	120	106	190	220
La	32.3	33.4	27	23.1	24.1	30.8	30	28.8	26	14
Ce	62.9	67.7	54.2	50.5	48.3	59.5	64.5	60	60	25
Pr	7	7.53	6.37	6.45	5.41	7.16	7.76	6.98		
Nd	27.1	30.6	22.4	25.4	20.6	27.9	27.6	28.9		
Sm	4.77	6.12	5.28	5.15	4.31	5.43	6.76	5.87		
Eu	1.06	1.40	1.15	1.01	0.95	1.19	1.36	1.47		
Gd	4.47	6.76	5.31	4.65	4	5.64	5.71	6.14		
Tb	0.65	0.94	0.73	0.68	0.60	0.82	0.81	0.88		
Dy	4.07	5.94	4.25	3.93	3.40	5.74	5.40	5.40		
Ho	0.85	1.18	0.86	0.87	0.65	1.08	1.05	1.13		
Er	2.32	3.55	2.57	2.47	2.04	3.16	2.88	3.13		
Tm	0.36	0.55	0.40	0.38	0.33	0.48	0.44	0.48		
Yb	2.51	3.87	2.68	2.44	2.14	3.47	2.97	3.22		
Lu	0.38	0.54	0.44	0.41	0.33	0.53	0.43	0.48		
(La/Yb)n	5.29	5.82	6.79	6.38	8.08	7.59	6.69	6.03		
Eu/Eu*	0.70	0.67	0.66	0.63	0.17	0.70	0.67	0.75		
∑REEs	150.7	170	133.6	127.3	117.2	152.9	157.6	152.9		

Table 1. (Continued).

Sample	Granitoids										
	SP-7	SP-101	BP-101	SP-22	BP-13	R15908*[1]	R15958*	R15918*	R15910*	R15915*	R15909*
	7	7	7	7	7	7	7	7	7	7	7
(Wt. %)											
SiO_2	63.31	66.55	63.68	61.23	65.98	62.30	66.44	65.33	63.42	66.41	71.81
TiO_2	0.65	0.87	0.62	0.64	0.60	0.63	0.45	0.49	0.59	0.46	0.26
Al_2O_3	15.35	14.18	14.92	14.85	14.98	16.02	15.24	15.53	15.37	15.22	13.77
Fe_2O_3	0.56	0.58	0.50	0.50	0.45	0.53	0.39	0.45	0.54	0.39	0.22
FeO	4.55	4.68	4.05	4.05	3.60	4.32	3.13	3.62	4.37	3.16	1.80
MnO	0.12	0.23	0.13	0.42	0.09	0.09	0.08	0.08	0.10	0.06	0.03
MgO	2.82	3.78	3.15	3.24	2.01	1.93	1.39	1.65	2.36	1.41	0.70
CaO	3.29	0.66	2.49	1.93	2.09	4.51	3.39	3.37	4.71	3.23	2.04
Na_2O	3.36	5.08	4.68	4.23	4.04	3.81	3.63	3.70	3.34	3.89	3.10
K_2O	3.61	0.97	3.65	4.07	3.90	2.75	3.21	3.23	3.39	2.83	4.62
P_2O_5	0.25	0.25	0.28	0.54	0.20	0.18	0.12	0.14	0.17	0.13	0.06
LOI	1.47	1.52	1.23	2.25	1.48	1.03	1.77	1.61	1.37	1.61	2.04
Total	99.34	99.35	99.38	97.95	99.42	98.75	99.94	99.77	100.38	99.32	100.80
A/CNK	1	1.34	0.92	1	0.94	0.92	0.96	0.99	0.87	0.99	0.99
(ppm)											
Ba	667	276	707	808	662	515	530	515	440	595	580
Be	1	2	<1	<1	3						

Table 1. (Continued).

Rb	73	21	71	109	77	59	80	88	103	62	145
Sr	340	128	259	191	347	342	269	288	315	273	188
Ga	17	12	16	16	16	18	16	17	16	15	13
Ta	0.8	0.8	0.8	0.7	0.9						
Th	8.9	9.4	9.9	9.5	12.1	5.3	10.9	10.1	10.7	10.8	17.6
U	1.5	1.9	2.4	2.5	2.9	0.9	1.5	2.3	1.8	3.1	4.6
Zr	257	203	243	201	232	198	170	174	180	180	148
Hf	6	6	6	5	6	4.8	9.4	4.6	4.9	4.6	4
Y	25	23	31	24	31	22	22	22	23	22	16
Cs	3	1	1	3	2	0.9	1.2	2.7	5	2.6	5
Nb	11	10	12	11	14	8	8	8	8	8	8
Co	8	6	5	7	7						
V	94	69	93	86	73	96	58	78	108	62	30
La	29.1	23.8	26.3	32.3	33.4	17.4	25	22	22	21.5	24.5
Ce	55.8	50.5	57.2	62.9	67.7	36.5	50	44	45	42.5	45.5
Pr	6.44	5.36	7.17	7	7.53						
Nd	22.5	20.9	25.3	27.1	30.6	17.4	20.5	18.2	20	17.6	15.8
Sm	4.54	4.04	6.03	4.77	6.12	4	3.4	4	4.2	3.9	3.3
Eu	0.97	1.06	1.29	1.06	1.40	1.11	0.94	0.87	0.93	0.87	0.57
Gd	4.40	3.95	5.24	4.47	6.76	3.60	3	3.70	3.80	3.60	3.30
Tb	0.62	0.57	0.79	0.65	0.94	0.54	0.50	0.65	0.65	0.62	0.55
Dy	4.21	3.67	4.30	4.07	5.94						
Ho	0.79	0.66	0.96	0.85	1.18	0.75	0.65	0.90	0.95	0.95	0.80
Er	2.31	2.25	3.14	2.32	3.55						
Tm	0.38	0.34	0.45	0.36	0.55						
Yb	2.66	2	3.09	2.51	3.87	2.10	2.35	2.30	2.15	2.40	1.90
Lu	0.42	0.36	0.52	0.38	0.54	0.34	0.39	0.37	0.35	0.38	0.29
(La/Yb)n	5.96	5.68	6.67	5.29	5.82	5.60	7.19	6.46	6.91	6.05	8.71
Eu/Eu*	0.66	0.81	0.70	0.70	0.67	0.88	0.88	0.68	0.69	0.70	0.52
∑REEs	135.1	119.5	141.8	150.7	170	83.74	106.73	96.99	80.55	94.32	96.51

Table 1. (Continued).

Sample	K-feldspar granite					
	SP-2	SP-3	SP-18	SP-26	R15900*[2]	R15914*
	[8]	[8]	[8]	[8]	[8]	[8]
(wt.%)						
SiO_2	75.94	73.88	75.22	75.75	76.75	76.97
TiO_2	0.18	0.26	0.23	0.20	0.19	0.15
Al_2O_3	13.29	13.27	13.32	12.61	11.70	11.70
Fe_2O_3	0.09	0.18	0.15	0.17	0.10	0.07
FeO	0.75	1.44	1.23	1.39	0.79	0.60
MnO	0.02	0.04	0.03	0.03	0.01	0.01
MgO	0.08	0.47	0.19	0.09	0.30	0.14

Table 1. (Continued).

CaO	0.13	0.14	0.25	0.51	0.51	0.43
Na_2O	3.31	3.70	3.77	3.82	2.85	2.63
K_2O	5.37	5.43	4.87	4.34	5.61	5.59
P_2O_5	0.05	0.03	0.06	0.03	0.02	0.01
LOI	0.58	0.73	0.41	0.76	0.74	1.76
Total	99.79	99.57	99.73	99.71	99.83	100.21
A/CNK	1.16	1.09	1.12	1.10	1.01	1.05
(ppm)						
Ba	445	655	635	643	170	140
Be	1	2	2	1		
Rb	151	128	120	74	200	207
Sr	54	65	73	99	50	36
Ga	14	13	13	14	11	11
Ta	1.1	1.3	1.2	1.3		
Th	21.9	14.9	16.2	16.4	30	31
U	2.3	3.2	2.7	2.9	5.6	3.4
Zr	147	193	199	168	134	112
Hf	5	7	7	7	5	4
Y	36	39	36	33	31	20
Cs	1	1	1	1	3.3	4.4
Nb	15	15	16	14	14	10
Co	0.4	1	1	0.6		
V	21	13	13	7	8	4
La	28.2	45.5	39.8	41.5	31	32
Ce	63.1	89.3	79.5	87	68	64
Pr	7.63	9.45	9.03	8.81		
Nd	26.8	32.9	37.3	29.9	27.5	23.5
Sm	6.12	7.19	6.23	5.62	5	4.30
Eu	0.52	0.83	0.63	0.65	0.30	0.27
Gd	5.87	6.52	6.07	6.01	5.1	3.60
Tb	0.85	1.03	0.89	0.94	0.95	0.69
Dy	5.68	6.97	5.67	6.17		
Ho	1.16	1.22	1.26	1.24	1.30	0.85
Er	3.52	3.31	3.51	3.39		
Tm	0.54	0.56	0.58	0.57		
Yb	3.91	3.70	3.88	3.90	3.60	2.50
Lu	0.52	0.55	0.58	0.56	0.53	0.35
(La/Yb)n	6.01	3.79	5.65	7.17	5.82	8.65
Eu/Eu*	0.27	0.37	0.31	0.34	0.18	0.20
∑REEs	154.4	209.2	194.9	196.3	143.3	132.1

[1]qz gabbro-monzodiorite, [2]diorite/qz diorite/ qz monzodiorite, [3]qz monzodiorite/monzonite, [4]qz monzonite/granite, [5]qz monzodiorite/ granodiorite, [6]tonalite/granodiorite, [7]monzogranite to syenogranite, [8]K-feldspar granite. *Data from Soltani (2000).

Table 2. Results of U-Pb-Th laser-ablation multicollector ICP mass spectrometry analysis of zircon of the hornblende-biotite quartz monzonite of Nay granitoids.

Sample	U (ppm)	Th (ppm)	U/Th	$^{207}Pb/^{206}Pb$	± (%)	$^{207}Pb/^{235}U$	± (%)	$^{206}Pb/^{238}U$	± (%)	Age
1	5.70	6.64	0.86	0.0485	7.3	0.0450	2.9	0.0067	2.9	43.2
2	1.70	1.30	1.31	0.0548	30.7	0.0557	6.7	0.0074	6.7	47.4
3	4.78	5.96	0.80	0.2071	11.3	0.2361	3.8	0.0083	3.7	53.0
4	4.88	2.59	1.88	0.0481	2.7	0.0419	2.4	0.0063	2.3	40.6
5	2.04	1.05	1.94	0.0485	3.0	0.0423	3.8	0.0063	3.8	40.6
6	1.52	1.12	1.36	0.0499	3.6	0.0434	4.8	0.0063	4.7	40.5
7	3.24	3.53	0.92	0.0485	5.0	0.0421	8.2	0.0063	8.2	40.4
8	1.56	9.10	0.17	0.0482	2.6	0.0417	1.3	0.0063	1.2	40.3
9	2.00	1.25	1.60	0.0479	12.0	0.0413	3.0	0.0063	2.9	40.2
10	1.63	1.23	1.33	0.0491	2.2	0.0423	1.3	0.0063	1.2	40.2

Table 3. Whole-rock Rb-Sr and Sm-Nd isotope compositions of the Nay granitoids.

Sample	Rb	Sr	$^{87}Rb/^{86}Sr$	$(^{87}Sr/^{86}Sr)i$	Sm (ppm)	Nd (ppm)	$^{147}Sm/^{144}Nd$	$(^{143}Nd/^{144}Nd)i$	εNdi	T_{DM} (Ma)	$f_{Sm/Nd}$
SP-7	72.7	340	0.62	0.705761	4.54	22.5	0.122	0.512502	–1.65	850	–0.38
BP-11	94.6	393	0.70	0.705346	5.43	27.9	0.118	0.512575	–0.22	710	–0.40
SP-18	120	73	4.74	0.706156	6.23	37.3	0.101	0.512586	–0.02	600	–0.49

for zircon U-Pb analysis in a previous article (Samiee et al., 2016).

4.3. Whole-rock Sr-Nd isotopes

Three whole-rock samples of the Nay granitoids (BP-11, SP-7, and SP-18) were analyzed for Sr and Nd isotopic compositions at the Isotope Geology Laboratory of the University of Aveiro, Portugal (Table 3). The analytical procedures correspond to those described for whole-rock Sr and Nd isotope analysis in several previous articles (e.g., Arjmandzadeh et al., 2011). During this analytical work, the SRM-987 standard yielded an average value of $^{87}Sr/^{86}Sr = 0.710264 \pm 0.000015$ (N = 13; conf. lim. = 95%) and the JNdi-1 standard gave $^{143}Nd/^{144}Nd = 0.5121015 \pm 0.0000074$ (N = 12; conf. lim. = 95%).

5. Geochemistry

5.1. Major elements geochemistry

Representative whole-rock analyses of the IRN bodies are presented in Table 1. IRN intrusives have a broad range of SiO_2 contents from 50.8 to 76.9 wt.% (Table 1). The sodic nature of these rocks is defined by the high Na_2O/K_2O (1.4 wt.%) and Na_2O+K_2O (8.7 wt.%) values (Table 1).

In the K-feldspar granite samples (SiO_2 of >72 wt.%), K_2O content is greater than Na_2O content and the mean K_2O/Na_2O ratio is 1.7 (Table 1). IRN bodies plot mainly in the quartz gabbro/diorite, quartz monzodiorite/monzonite, granodiorite, granite, and K-feldspar granite fields on the Middlemost (1985) diagram (Figure 4A). On the K_2O vs. SiO_2 diagram (Peccerillo and Taylor, 1976), they plot in the tholeiite and calc-alkaline to mainly high-K calc-alkaline and shoshonitic fields (Figure 4B).

In the Th-Co diagram (Hastie et al., 2007), the IRN rocks plot in the high-K calc-alkaline and shoshonitic series domains (Figure 4C). On the Al saturation index diagram (Shand, 1943) (Figure 4D), IRN bodies are mainly metaluminous to weakly peraluminous and the Al saturation index (ASI: molar $Al_2O_3/(CaO+Na_2O+K_2O)$) is <1.1 (Table 1), but 3 samples (quartz, monzogabbro, and quartz monzonite/monzonite) are highly peraluminous (ASI = 1.33–2.32; Figure 4D and Table 1). These 3 samples also have the minimum SiO_2 and CaO and maximum Al_2O_3 and MgO contents and show characteristics of tholeiitic magma. The tholeiitic magmas were emplaced at the first stage of magmatic activity. Some characteristics, such as A/CNK of <1 and $Na_2O > K_2O$, are similar to those of I-type rocks (White and Chappell, 1983), which is further supported by the presence of index modal minerals such as hornblende and titanite.

The Nay granitoids define the calc-alkaline to alkali-calcic field in the modified SiO_2 vs. alkali lime index

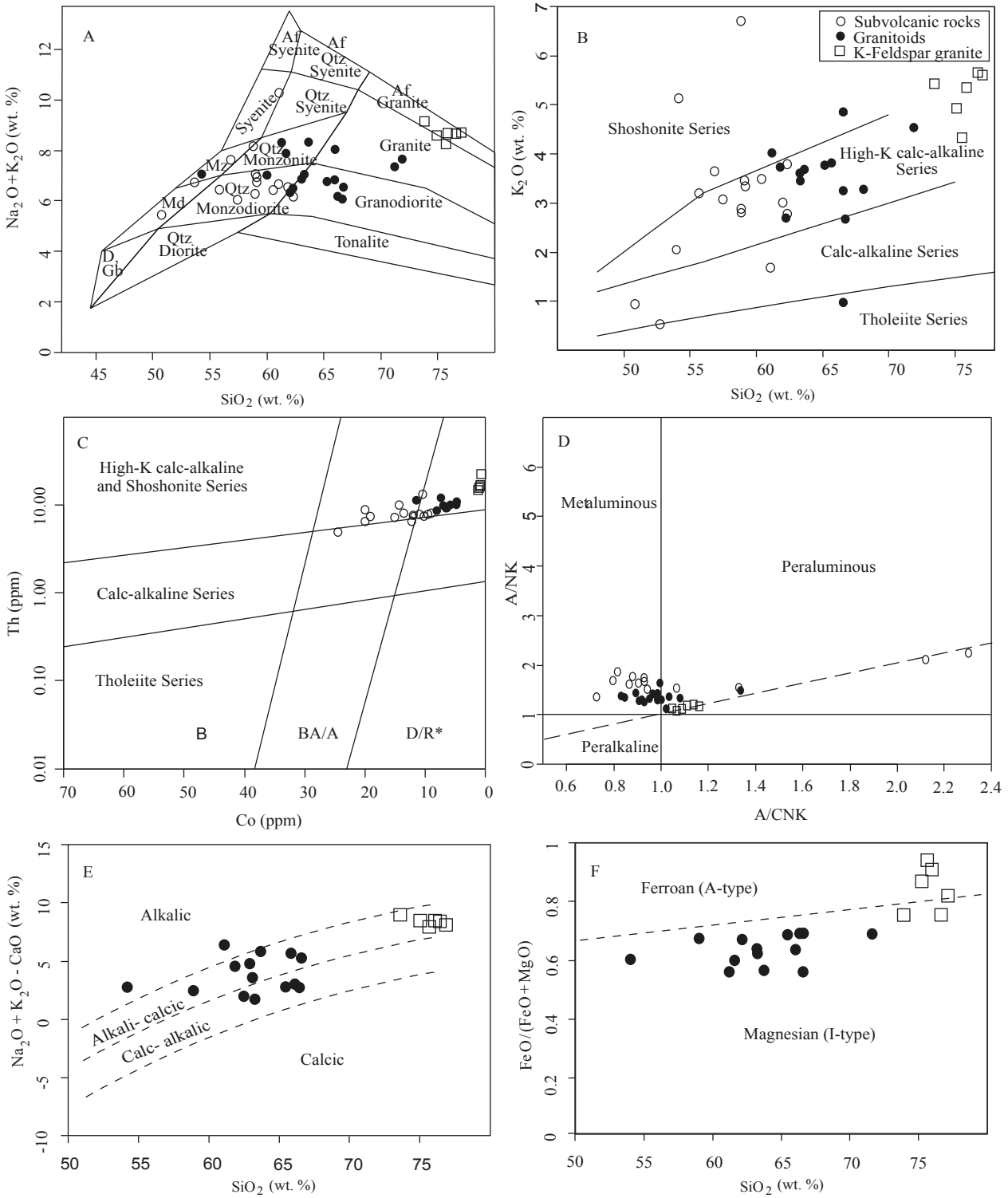

Figure 4. Geochemical classification of the IRN bodies. (A) $Na_2O + K_2O$ vs. SiO_2 diagram. Fields after Middlemost (1985). (B) K_2O vs. SiO_2 diagram; fields defined by Peccerillo and Taylor (1976). (C) Plot of Nay intrusives in the Th-Co diagram; fields after Hastie et al. (2007). Subhorizontal boundaries separate fields of magma series typical of subduction-related settings. Subvertical boundaries separate fields of volcanic rocks in those settings. (D) A/NK vs. A/CNK [ANK = molar $Al_2O_3/(Na_2O+K_2O)$ and ACNK = molar $Al_2O_3/(CaO+Na_2O+K_2O)$ (Shand, 1943). (E) Plots of the Nay granitoids on modified alkali lime index ($Na_2O + K_2O–CaO$) vs. SiO_2 discrimination diagram (Frost and Frost, 2011). (F) Plots of the Nay granitoids on the SiO_2 vs. $FeO_t/FeO + MgO$ discrimination diagram (Frost et al., 2001).

($Na_2O+K_2O–CaO$) diagram proposed by Frost and Frost (2011; Figure 4E). While the majority of granitoid samples plot in the magnesian (I-type) field on the SiO_2 vs. FeO/(FeO+MgO) discrimination diagram (Frost et al., 2001), the relatively K-feldspar granitic samples plot in the ferroan (A-type) domain (Figure 4F).

All samples display relatively linear trends for most major and minor elements vs. SiO_2 on the Harker variation plots (Figure 5). In all rock types, CaO, MgO, TiO_2, and P_2O_5 display negative correlations with silica (Figure 5). The crystallization of ilmenite, magnetite, titanite, and apatite decreases the Ti and P in the residual magma. The observed geochemical features document the role of fractional crystallization in the magmatic evolution.

Ba, Zr, Nb, Sr, and Y behave incompatibly in the magmas generating the mafic series, but compatibly in felsic series as specified by curved trends. Negative correlations of some trace elements (e.g., Co and V) with increasing SiO_2 demonstrate compatible behavior, whereas positive correlations (e.g., La) point to incompatible behavior (Figure 5).

On the Rb vs. Ta + Yb and Rb vs. Y + Nb tectonomagmatic diagrams (Pearce et al., 1984; Pearce, 1996), all rocks fall in the "postcollision granite" domain (Figures 6A and 6B), which further attests to the I-type characteristic of Nay granitoids.

5.2. Trace and rare earth elements geochemistry

The subparallel pattern of the IRN bodies is noteworthy on the chondrite-normalized REE diagram (Figure 7). These intrusives are enriched in some large ion lithophile elements (Rb, Cs, Ba, and K) and those incompatible elements that behave similarly to LILEs (Th and U). Primitive mantle normalized multielement spider diagrams indicate that these rocks are enriched in light REEs such as La and Ce [$(La/Yb)_N$ = 3.79–8.71], but extreme depletion in high field strength elements is evident (e.g., Nb and Ti) (Figure 7). High Y contents (>13 ppm) suggest a source dominated by amphibolite (Rapp et al., 1999).

Moreover, IRN intrusives display relatively unfractionated flat heavy REE (HREE) patterns [$(Gd/Yb)_N$ = 1.12–1.69]. All samples have a negative Eu anomaly [$(Eu/Eu^*)_N$ = 0.17–0.88]. All granitoid samples are slightly enriched in LREEs. Some elements such as Cs, Zr, and P are more depleted in K-feldspar granite. Such characteristics are attributed to the high fractionation process, where the separation of some minerals such as titanite and allanite generates end-members of the magmatic suite (K-feldspar granite) that are poor in some elements such as Zr, Cs, Ce, Nb, and P (DePaolo, 1981).

6. Zircon U-Pb dating

The age of the Nay granitoids (hornblende-biotite quartz monzonite; sample BP-11) was obtained using zircon U-Pb geochronology. The U-Pb zircon data are available in Table 2 and presented as concordia and average age graphics in Figure 8. The zircon crystals are generally automorphic, pale yellowish or colorless, and transparent. The crystals range in size from 50 to 300 μm and have a length/width ratio of 1:1–5:1.

Ten analyzed zircon points from hornblende-biotite quartz monzonite defined a mean age (weighted mean) of 40.2 ± 0.3 Ma (Table 2; 10 analyzed points, 2σ errors). The zircon U/Th ratio is important to define metamorphic and magmatic zircons. U/Th values in metamorphic (inherited) and magmatic zircon are 5.0 to 10 and <5.0, respectively (Rubatto et al., 2001; Williams, 2001; Rubatto, 2002; Sun et al., 2002; Wu and Zheng, 2004). The magmatic origin for zircon crystals is confirmed by identical and moderately uniform U/Th ratios (cores: 0.86–1.88; rims: 0.17–1.94; Table 2) and their respective spot U-Pb ages (Table 2), and no postmagmatic processes or inherited components were observed.

Considering these features along with the high closure temperatures for zircon crystals, Cherniak and Watson (2000) suggested the U-Pb isotopic data as indicative of the crystallization ages of the intrusives. Since field observation and crosscutting relationships indicate that all three groups of intrusives were generated in a limited time span, the obtained zircon U-Pb age testifies that these rocks probably intruded in middle Eocene time.

7. Whole-rock Sr-Nd isotopes

Sr-Nd isotopic data of the Nay granitoids are presented in Table 3 and plotted in Figure 9. Three samples from the Nay granitoids, including hornblende-biotite quartz monzonite (BP-11), hornblende monzogranite (SP-7), and K-feldspar granite (SP-18), were analyzed for Sr and Nd composition. The initial $^{87}Sr/^{86}Sr$ values for granitoids were calculated at 40 Ma and range between 0.7053 and 0.7061 (Table 3).

The Sm-Nd isotopic compositions confirm essentially uniform εNd values from –1.65 to –0.02 calculated at 40 Ma (Table 3), which support a comagmatic origin for all the IRN granitoids. The Nd model ages (T_{DM}; DePaolo, 1981) cluster tightly around 0.80–0.60 Ga for Nay granitoids, similar to both the inherited zircons from Kashmar pluton (Shafaii Moghadam et al., 2015) and the formation age of Cadomian granites within central Iran (Ramezani and Tucker, 2003), suggesting an age of at least ~0.6 Ga for the origin during partial melting and generation of Nay I-type granites and that older continental crust or lithosphere was included in generating the granitic magmas.

Jahn (2004) suggested that T_{DM} may result from either Sm/Nd fractionation during magma differentiation or between the granitic melt and its origin during partial melting. Furthermore, the young and narrow extent of

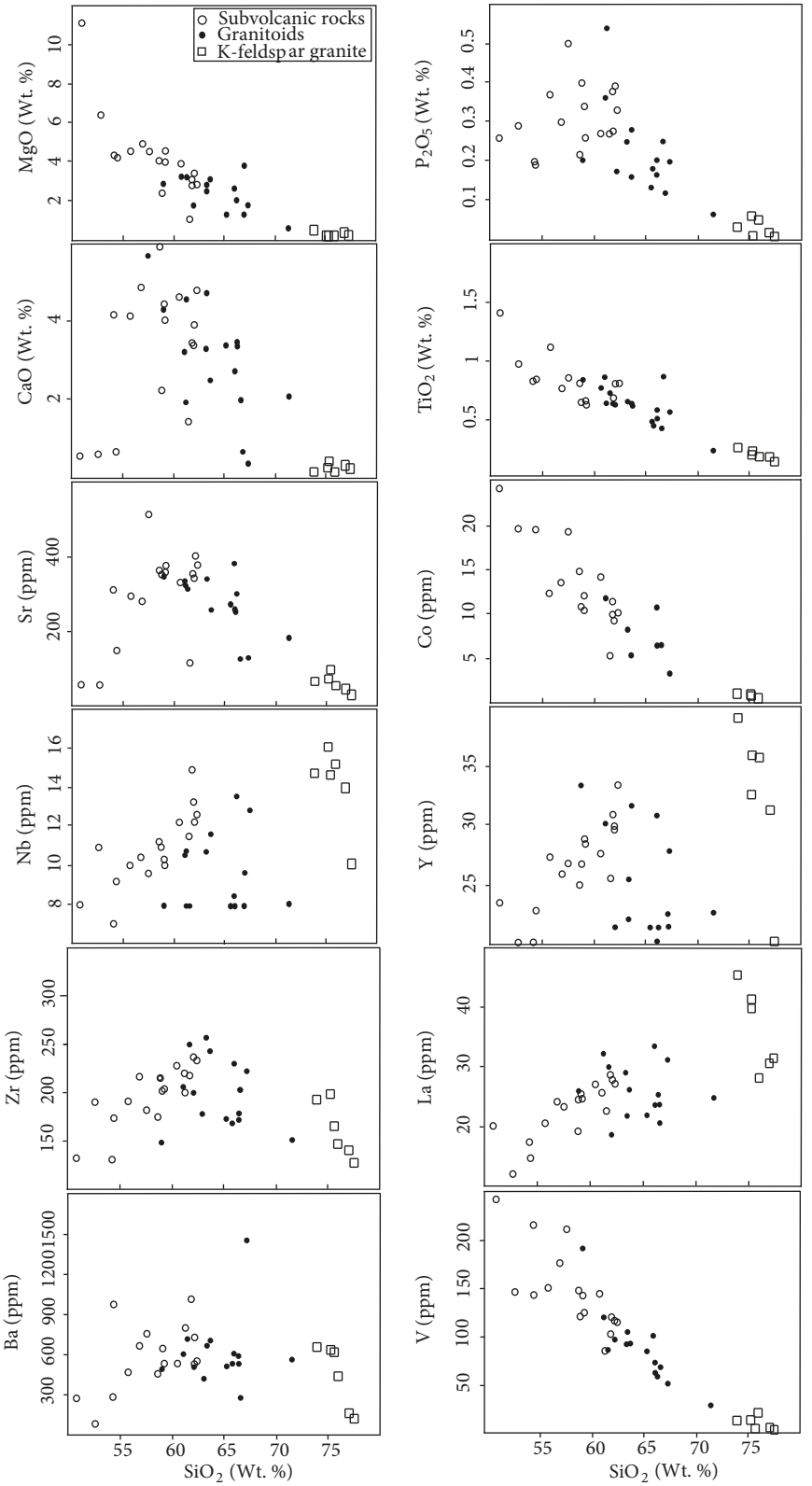

Figure 5. Harker diagrams illustrating selected major and trace elements for the IRN bodies.

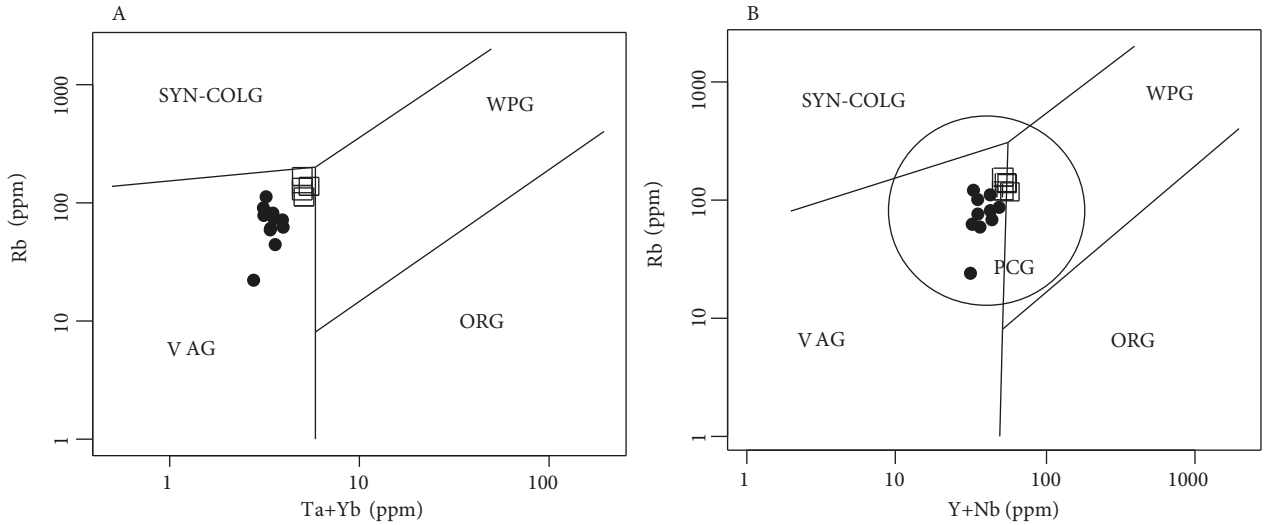

Figure 6. Tectonic discrimination diagrams for the Nay granitoids (Pearce et al., 1984). (A) Rb vs. Ta + Yb; (B) Rb vs. Y + Nb; field of postcollisional granite (PCG) defined by Pearce (1996). VAG: Volcanic arc granite; WPG: within plate granite; Syn-COLG: syncollision granite; ORG: ocean ridge granite; PCG: postcollision granite.

T_{DM} ages, covering $f_{Sm/Nd}$ values limited to –0.4 ± 0.2, is convincing support for considerable mantle involvement in the generation of Nay granitoids (Table 3).

On the $^{143}Nd/^{144}Nd$ vs. $^{87}Sr/^{86}Sr$ plot (Figure 9), the Nay granitoids plot in the Sr-enriched quadrant in the mantle array. This suggests an isotopic characteristic of enriched lithospheric mantle (ELM) with similar composition to postcollisional Eocene intrusive and volcanics in the Alborz (Aghazadeh, 2010; Asiabanha and Foden, 2012), Lut-Sistan (Pang et al., 2013), and Urumieh-Dokhtar (Omrani et al., 2008; Ahmadian et al., 2009; Verdel et al., 2011) magmatic zones of Iran and many cases including postcollisional Eocene intrusive and volcanic rocks in the southern part of the Eastern Pontides and Torul as well as a K-enriched subcontinental lithospheric mantle (SCLM) source of postcollisional volcanic rocks in western Anatolia (Keskin et al., 2008; Dilek et al., 2010; Kaygusuz, 2011; Arslan et al., 2013; Gülmez et al., 2013; Aslan et al., 2014; Kasapoğlu et al., 2016; Temizel et al., 2016; Ersoy et al., 2017; Yücel et al., 2017; Göçmengil et al., 2018) (Figure 9). The distinction possibly indicates that the Cadomian aged (Ediacaran–Cambrian) lithosphere was considerably the origin of Nay granitoids.

8. Discussion

8.1. Petrogenesis

The plot of subvolcanic samples (mafic) in the Tb_N/Yb_N vs. Th (ppm) variations diagram with the horizontal line separating fields for garnet-bearing lherzolite (high Tb_N/Yb_N) and spinel-bearing lherzolite (low Tb_N/Yb_N) (e.g., Wang et al., 2002) suggests that mafic magmas formed in the presence of residual spinel and rare garnet (Figure 10A). In La/Sm vs. La (ppm) and Yb vs. La/Yb diagrams (Figures 10B and 10C; Temizel et al., 2016), the mafic rocks have high and low amounts of incompatible La and Sm, respectively.

None of the La or Sm is influenced considerably by variations in source mineralogy (e.g., garnet or spinel), thus providing evidence on the bulk chemical features of the source. All mafic samples have La abundances and La/Sm ratios greater than those generated by melting of a depleted mantle (DM; McKenzie and O'Nions, 1991) or a primitive mantle (PM; Sun and McDonough, 1989) composition. Therefore, the E-MORB mantle composition defined by McDonough and Sun (1995) is considered as a starting material that melted from 5% to 10% under spinel as well as under garnet lherzolite field conditions.

The partial melting trajectories (Figure 10B; Temizel et al., 2016) that coincide with the Nay mafic rocks imply 5%–10% partial melting of the metasomatized mantle source and are characterized by La abundances and La/Sm ratios enriched relative to the primitive mantle or depleted mantle. As shown in the La/Yb vs. Yb diagram (Figure 10C; Temizel et al., 2016), samples plot on a line defined by mixing between 1% melted spinel lherzolite and 0.5% melted garnet lherzolite, which is correlated to 55%–80% melt of a spinel lherzolite and 20%–45% melt of a garnet lherzolite (the theoretical mixing proportions). This suggests that the melts for the Nay subvolcanic rocks may have been produced by variable amounts of melting in spinel and garnet lherzolite (Figures 10B and 10C). The variable proportion of melts generated and incorporated at different mantle depths is most likely the consequence of melt processes related to an upwelling asthenospheric mantle.

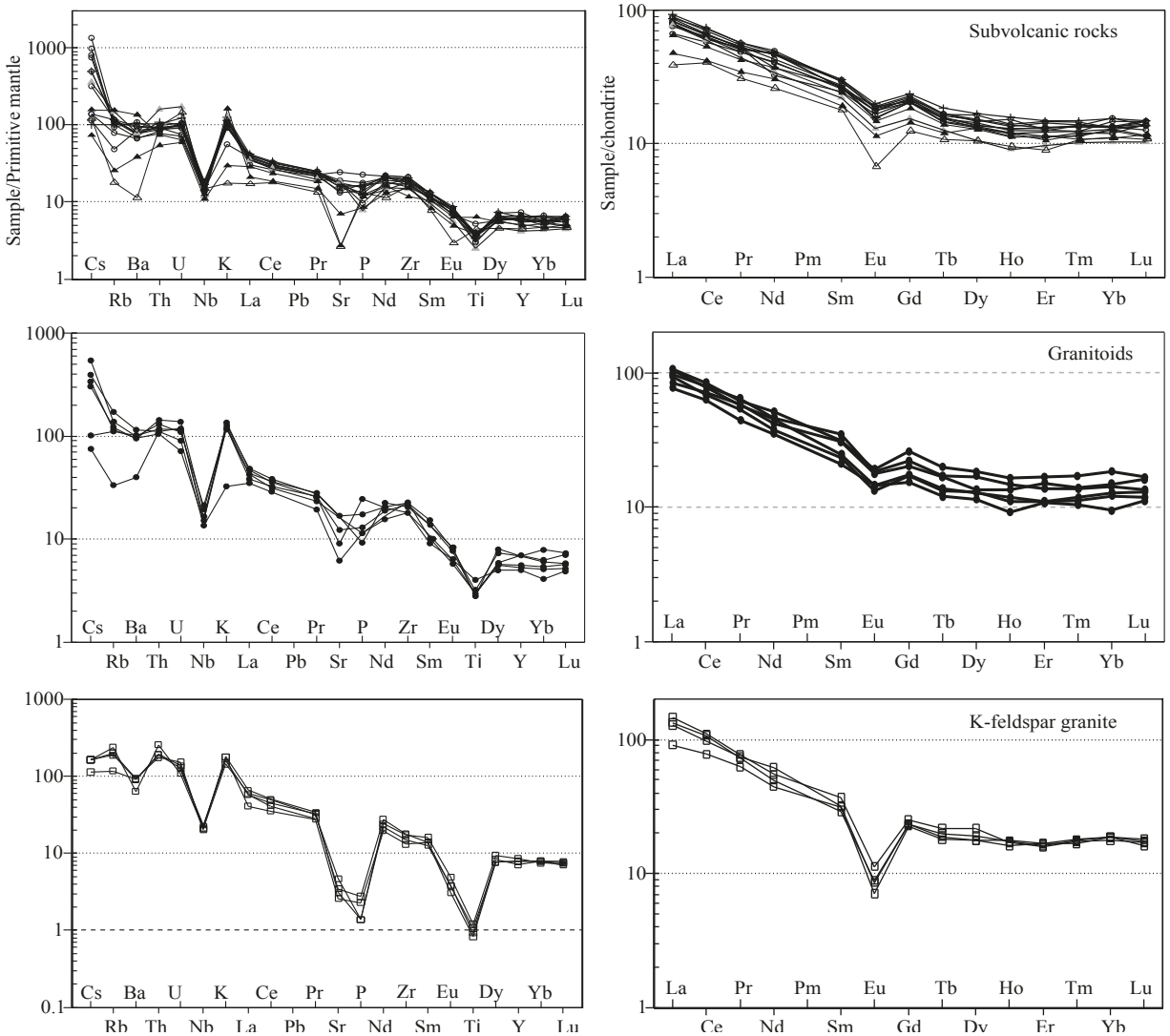

Figure 7. Multielement and REE diagrams for different Nay intrusive rocks. Normalizing values are from Sun and McDonough (1989).

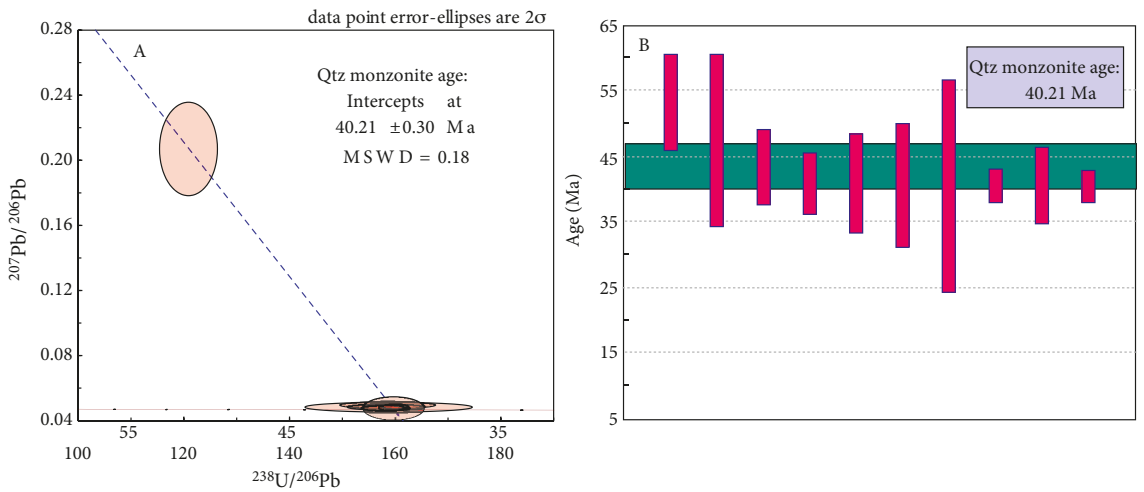

Figure 8. Zircon U-Pb dating of representative rock sample (hornblende-biotite quartz monzonite) from the IRN granitoids. (A) Concordia diagram. (B) Average age plot.

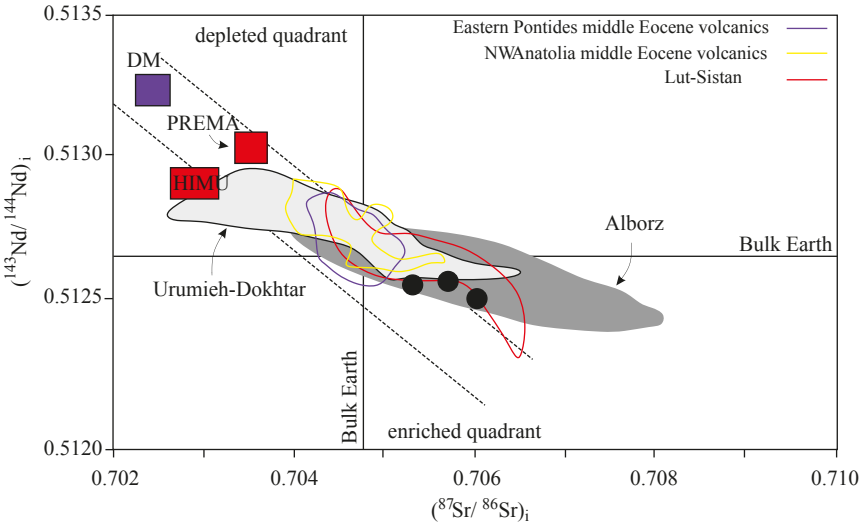

Figure 9. Initial $^{143}Nd/^{144}Nd$ vs. $(^{87}Sr/^{86}Sr)_i$ for Nay granitoids compared with Eocene-Miocene magmatic belt rocks from Iran and Turkey. Data for Eocene-Oligocene magmatic rocks from the Urumieh-Dokhtar region, southwestern Iran, from Omrani et al. (2008), Ahmadian et al. (2009), and Verdel et al. (2011). Data for Alborz region, northern Iran, from Aghazadeh et al. (2010) and Asiabanha and Foden (2012); data for Lut-Sistan region, eastern Iran, from Pang et al. (2013). Data from Eocene volcanic rocks from NW Anatolia (Aydınçakır and Şen, 2013; Gülmez et al., 2013; Kasapoğlu et al., 2016) and middle Eocene volcanics from the Eastern Pontides (Kaygusuz et al., 2011; Temizel et al., 2012, 2016; Arslan et al., 2013; Aslan et al., 2014; Yücel et al., 2017; Göçmengil et al., 2018). Mantle reservoirs were taken from Zindler and Hart (1986). DM: Depleted mantle, HIMU: high μ mantle (mantle with high U/Th ratio), PREMA: prevalent mantle. Data for lithospheric mantle array from Davies and von Blanckenburg (1995).

The IRN intrusives are metaluminous to highly peraluminous and range in composition from tholeiitic to high-K calc-alkaline and shoshonitic. They are moderately enriched in light REEs [$(La/Yb)_N$ = 3.79–8.71] and LILEs (such as Ba, Th, Rb, U, and K) and depleted in HFSEs. The presence of negative europium anomalies and relatively flat heavy REE patterns are proven by [$(Eu/Eu^*)_N$ = 0.17–0.88] and [$(Gd/Yb)_N$ = 1.12–1.69] values. While depletion in Nb-Ta-Ti elements and Ba, Th, Rb, U, Pb, and K enrichments are signatures of arc-related magmatic rocks (Pearce and Parkinson, 1993; Reagan and Gill, 1989; Martin, 1994, 1999), LILE enrichments and HFSE depletions are also quite common in syn- to postcollisional rocks (Pearce et al., 1984).

High-K calc-alkaline granites are not common in anorogenic environments but are widespread in convergent margin settings, especially in postcollisional regions (e.g., Kemp et al., 2009). The field characteristics, mineral composition (magnetite, biotite, and hornblende), and Sr-Nd isotope and geochemical compositions together indicate that all rock types are essentially comagmatic and belong to postcollisional I-type granites. The Sr-Nd isotopic data further indicate the influence of mantle magmas on old continental crust. Hildreth (1981) indicated that accumulation of mafic magmas at the base of the continental Moho may provide enough heat for partial melting of the lower crust. This process forms high-K calc-alkaline I-type granitoids that constitute variable proportions of the mantle and crustal materials.

Generally linear trends for most major, trace (Co and V), and rare earth (La) elements against SiO_2, and the compatible vs. incompatible behavior of Ba, Zr, Nb, Sr, and Y from mafic to felsic rocks, testify to the role of fractional crystallization in the evolution of magmas. Fractional crystallization (FC) and/or crustal assimilation (AFC) (DePaolo, 1981) of mantle-derived magmas and/or magma mixing between felsic and mafic magmas derived from crustal and mantle sources had an essential role in the magmatic evolution of the IRN bodies.

The unfractionated and flat HREE variations are characteristic of melting at pressures under the garnet stability domain (Henderson, 1984; Green, 1994). IRN intrusions show relatively low La/Yb ratios (3–9), negative Eu anomalies (Eu/Eu of <1), and less fractionated heavy REEs (Sm/Yb = 1–3; Gd/Yb = 1–2) (Figure 7 and Table 1), which reflects pyroxene and plagioclase fractionation from the melt. The CaO (wt.%) vs. Y (ppm) diagram (Figure 11) further supports this. Plagioclase and/or K-feldspar plays an important role in the generation of negative Eu anomalies during the fractional crystallization processes (Huang et al., 2008; Zhong et al., 2009). Accordingly, assimilation and fractional crystallization mechanisms (AFC) in the lower depths of the lithosphere are suggested to be responsible for magmatic evolution in Nay.

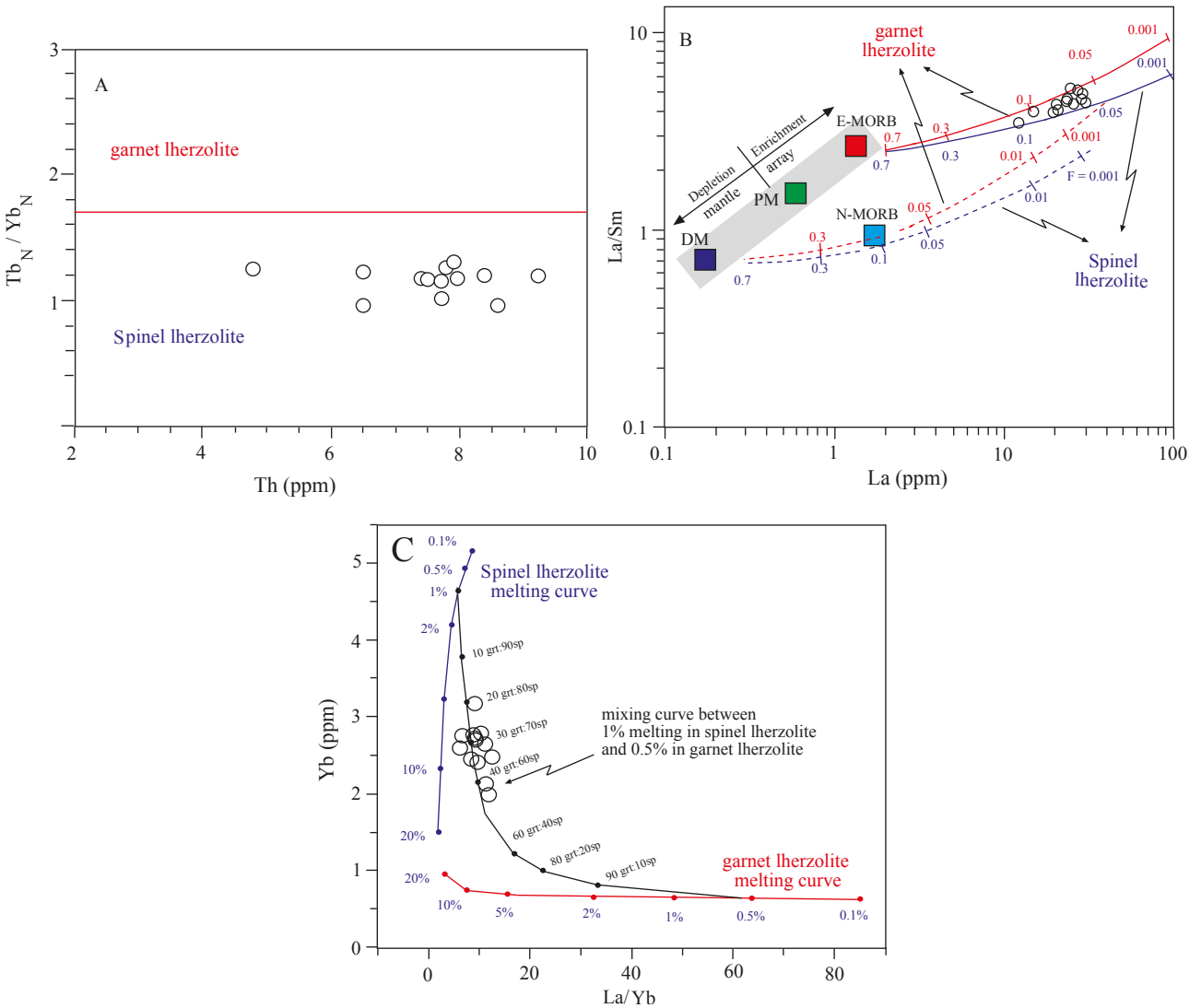

Figure 10. (A) Tb_N/Yb_N vs. Th plot for IRN bodies. Horizontal line separates domains defined for melting garnet- and spinel-lherzolite (Wang et al., 2002). (B) La vs. La/Sm adopted from Temizel et al. (2016) and (C) La/Yb vs. Yb plots adopted from Temizel et al. (2016) indicating drawn melt lines using the nonmodal batch melting equations of Shaw (1970) for the basic samples (SiO_2 < 50 wt.%). (C) Melt curves drawn for spinel-lherzolite (with mode and melt mode of $ol_{0.5}$ + $opx_{0.27}$ + $cpx_{0.17}$ + $sp_{0.11}$ and $ol_{0.06}$ + $opx_{0.28}$ + $cpx_{0.67}$ + $sp_{0.11}$, respectively; Kinzler, 1997) and for garnet-lherzolite (with mode and melt mode of $ol_{0.6}$ + $opx_{0.2}$ + $cpx_{0.1}$ + $gt_{0.1}$ and $ol_{0.03}$ + $opx_{0.16}$ + $cpx_{0.88}$ + $gt_{0.09}$, respectively; Walter, 1998). Mineral/matrix partition coefficients and depleted mantle (DM) are from the compilation of McKenzie and O'Nions (1991); PM, N-, and E-MORB compositions are from Sun and McDonough (1989). The bold line indicates the mantle array defined using DM, PM, and E-MORB compositions. Dashed and solid curves or lines are the melting trends from DM and E-MORB, respectively. Thick marks on the lines suggest the degrees of partial melting for a given mantle source. (D) Melt curves are drawn for spinel-lherzolite (with mode and melt mode of $ol_{0.578}$ + $opx_{0.27}$ + $cpx_{0.119}$ + $sp_{0.033}$ and $ol_{0.1}$ + $opx_{0.27}$ + $cpx_{0.5}$ + $sp_{0.13}$, respectively) and for garnet-lherzolite (with mode and melt mode of $ol_{0.598}$ + $opx_{0.211}$ + $cpx_{0.076}$ + $gt_{0.115}$ and $ol_{0.05}$ + $opx_{0.20}$ + $cpx_{0.30}$ + $gt_{0.45}$, respectively). Mineral/matrix partition coefficients are from the compilation of McKenzie and O'Nions (1991). The source is considered to be enriched mantle composition evolved from the primitive mantle composition defined by Taylor and McLennan (2009), namely La =1.2 × 0.546 ppm and Yb = 0.9 × 0.368 ppm. The curves represent mixing between small melt fractions within the garnet stability domain in the mantle and larger melt fractions within the spinel stability field of the mantle.

As mentioned above (Figure 5), linear correlations between trace elements and SiO_2 can provide additional evidence of fractional crystallization (FC) and/or crustal assimilation (AFC) (DePaolo, 1981) of mantle-derived magmas and/or magma mixing (Perugini and Poli, 2004) between felsic and mafic magmas derived from crustal and mantle sources. The hyperbolic array in the Rb/Sr vs. Ti/Zr and some linear correlations between Sr/Zr

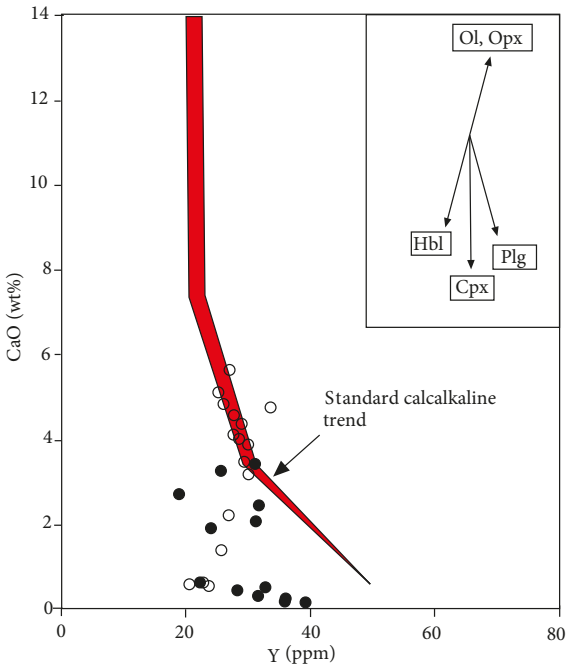

Figure 11. CaO (wt.%) vs. Y (ppm) plot for the IRN bodies. Shaded area represents the "standard" calc-alkaline trend of Lambert and Holland (1974). The vectors show qualitative trends of the effect of fractional crystallization of common silicates.

vs. Ti/Zr diagrams (Figures 12A and 12B; Kaygusuz et al., 2014) show mixing of two distinct geochemical end-members (i.e. mantle-derived magmas and lower crustal components).

The Sr-Nd isotopic features and trace element signatures of IRN bodies indicate their possible acquisition from mixing of the lower crust and mantle-derived magmas, followed by the AFC process.

To evaluate the possibility of source mixing in the parental magma of Nay granitoids, binary isotopic modeling (Langmuir et al., 1978; DePaolo and Wasserburg, 1979) was employed with the use of mantle and lower crustal end-members (Figure 12C). Plotting of the Nay granitoids suggests a magma mixing process. Sr-Nd modeling shows a mixed origin for Nay granitoids with parental magma involving ~18% to 27% of lower crustal-derived and ~73% to 82% of mantle-derived magmas (Figure 12C).

8.2. Tectonic implications

The geochemical, geochronological, and tectonic environment of Nay granitoids in the center of the KKBB is similar to that of the Sangan granitoids (Malekzadeh Shafaroudi et al., 2013) towards the east. They are meta-aluminous and high-K calc-alkaline to shoshonitic igneous rocks, formed in the postcollisional environment.

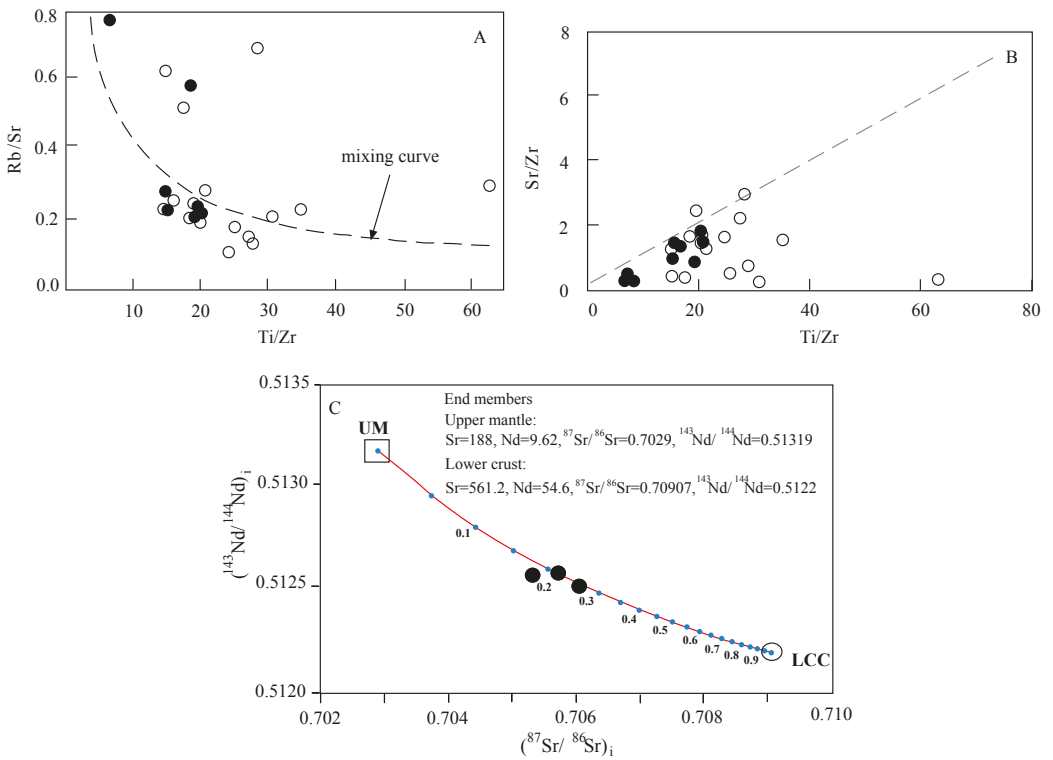

Figure 12. (A–B) Ti/Zr vs. Rb/Sr and Sr/Zr diagrams adopted from Kaygusuz et al. (2014) for IRN bodies; (C) $^{143}Nd/^{144}Nd_{(i)}$ vs. $^{87}Sr/^{86}Sr_{(i)}$ plot for Nay granitoids with simple source mixing lines between upper mantle (UM; Klein, 2004) and local lower crustal (LCC, gabbroic enclave of a Paleozoic pluton from Dokuz, 2011) end-members. Tick marks indicate *f* = fraction of UM in product magma, and are given in intervals of 0.1 to a maximum of 0.9.

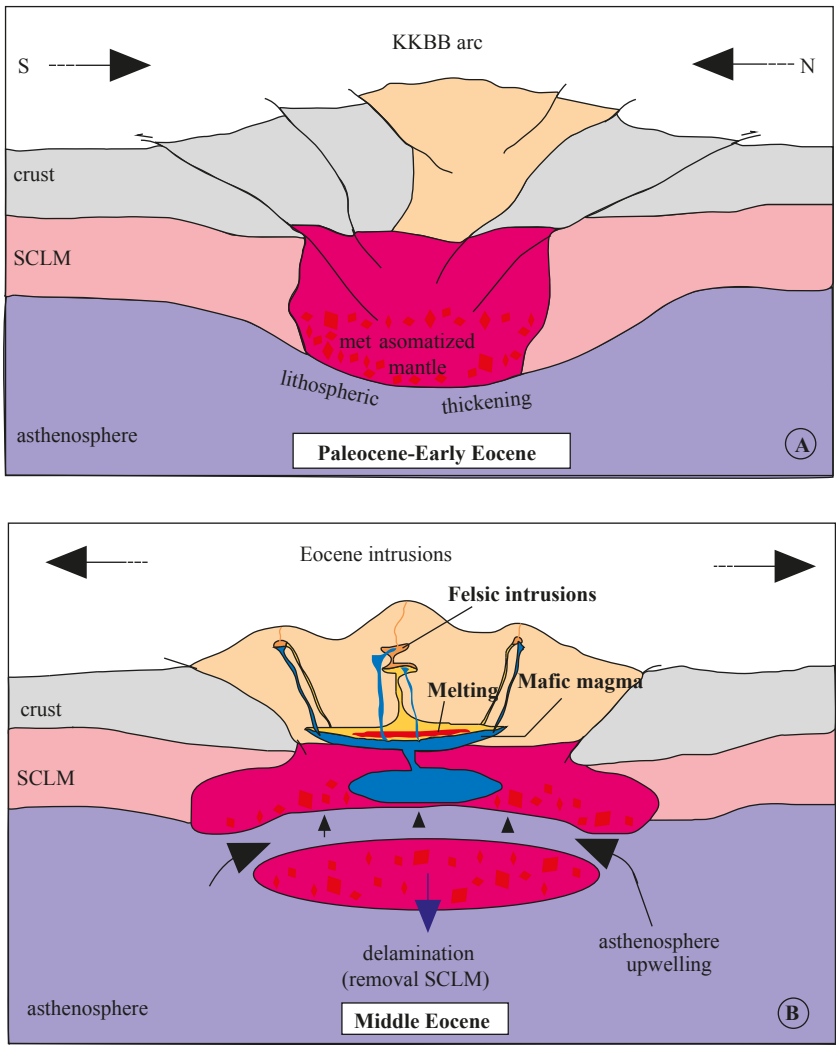

Figure 13. Schematic geodynamic model for the generation of Eocene IRN magmatism in the KKBB belt (modified after Aslan et al., 2014). (A) Continent-continent collision between the Eurasian plate in north (N) and Arabian platform in south (S) caused lithospheric thickening. (B) Delamination and removal of thickened lithospheric mantle caused melting of the thickened crust and produced postcollisional magmas.

The Nay and Sangan granitoids are related to a W-E trending batholith that outcrops throughout the belt. A conducive tectonic environment for generating I-type calc-alkaline granites is postcollisional extension following crustal thickening by continental collision and postorogenic collapse (e.g., Davies and Blanckenburg, 1995; Bonin, 2004; Jiang and Li, 2014). Such an environment has been suggested to form the Eocene magmatic rocks in the Lut-Sistan zone (Arjmandzadeh et al., 2011; Pang et al., 2013; Arjmandzadeh and Santos, 2014).

In general, a collisional orogenic belt (e.g., the Tibetan orogeny) usually underwent a three-stage tectonic evolution, i.e. main-collisional convergent, late-collisional transform, and postcollisional extension (cf. Hou and Cook, 2009). Three significant processes developed in syn-, late-, and postcollisional episodes, respectively: breaking off of the subducted Tethyan slab; large-scale strike-slip faulting, shearing, and thrusting; and delamination (or breaking off) of the lithosphere.

The geodynamic scenario for the initiation, spreading, and closure of the Neo-Tethyan basin ocean in the Iranian–Turkish Plateau was presented in Section 1. Our data are consistent with postcollisional processes (as mentioned above) after closing of the Neo-Tethyan arms in the Iranian–Turkish Plateau. Considering the whole dataset, we suggest that the Eocene IRN magmatism occurred as a postcollisional product by asthenospheric upwelling as a result of convective removal of the lithosphere during an extensional collapse of the central Iranian block.

After cessation of the Sabzevar subduction beneath the Lut block (Central Iranian block) (Stampfli and Borel, 2002; Moix et al., 2008; Verdel et al., 2011; Shafaii Moghadam et al., 2015), collision-driven slab breakoff magmatism occurred during the Eocene and Oligocene (Koop et al., 1982; Vincent et al., 2005; Allen and Armstrong, 2008; Agard et al., 2011; Ballato et al., 2011; Mouthereau et al., 2012) (Figure 13A).

The postcollisional extension regime and crustal thinning may have proceeded from enriched lithospheric mantle delamination that led to the asthenospheric upwelling, causing partial melting of the enriched lithospheric mantle and generating mafic magmas. These mafic magmas may have risen through the thickened lower crust and caused partial melting there, forming magma chambers. Continued magma mixing and AFC processes in the magma chambers may have generated consequent magmas developing the mafic to felsic intrusive rocks of Nay (Figure 13B).

9. Conclusions

Whole-rock and Sr-Nd isotopic geochemical data and geochronology from the Nay hypo-abyssal rocks in the northern part of the Lut block (NE Iran) shed new light on the origin and evolution of Middle Eocene intrusive rocks, enabling us to reach the following conclusions:

1) Zircon U-Pb geochronology of the granitoids reveals that felsic intrusive rocks were emplaced in Middle Eocene (Lutetian) time.

2) The Eocene granitoids are characterized by narrow initial $^{87}Sr/^{86}Sr$ values from 0.7053 to 0.7061 and $\varepsilon Nd_{(i)}$ values from –1.65 to –0.02.

3) Sr-Nd characteristics and trace REE element modeling of melts revealed that the parental magmas of Eocene intrusive rocks had isotopic characteristics of the ELM. Mixing of mantle magmas with a variable proportion of partial melting of spinel lherzolite and garnet lherzolite produces mafic melts.

4) Due to the extensional regime and crustal thinning and delamination, upwelling asthenosphere mantle provided the thermal anomaly, metasomatized the SCLM, and caused partial melting of thickened enriched lithospheric mantle. Fractional crystallization with assimilation (AFC) of produced magmas contributed to the postcollisional Eocene intrusive and volcanic rocks in the Nay area.

Acknowledgments

This research is a part of the first author's PhD dissertation at Ferdowsi University, Mashhad, Iran. The authors wish to thank Sara Ribeiro (Laboratorio de Geologia Isotopica da Universidade de Aveiro) for the TIMS analysis in the clean room. The authors are very grateful to Editor-in-Chief Dr Orhan Tatar and the two reviewers, Dr Gönenç Göçmengil and Dr Namık Aysal, for accurate, insightful, and valuable comments that significantly improved the manuscript.

References

Afsharharb A, Aghanabati A, Majdi B (1987). Geological Map of Mashhad, Scale 1:250000. Tehran, Iran: Geological Survey of Iran.

Agard P, Omrani, J, Jolivet L, Whitechurch H, Vrielynck B, Spakman W, Monie P, Meyer B, Wortel R (2011). Zagros orogeny: a subduction-dominated process. Geol Mag 148: 692-725.

Aghazadeh M, Castro A, Omran, NR, Emami MH, Moinvaziri H, Badrzadeh Z (2010). The gabbro (shoshonitic)–monzonite–granodiorite association of Khankandi pluton, Alborz Mountains. NW Iran. J Asian Earth Sci 38: 199-219.

Ahmadian J, Haschke M, McDonald I, Regelous M, Ghorbani MR, Emami MH, Murata M (2009). High magmatic flux during Alpine-Himalayan collision: Constraints from the Kal-e-Kafi complex, central Iran. Geol Soc Am Bull 121: 857-868.

Alaminia Z, Karimpour MH, Homam SM, Finger F (2013). The magmatic record in the Arghash region (northeast Iran) and tectonic implications. Int J Earth Sci 102: 1603-1625.

Alavi M (1996). Tectonostratigraphic synthesis and structural style of the Alborz mountain system in northern Iran. J Geodyn 21: 1-33.

Alavi M (2007). Structures of the Zagros fold-thrust belt in Iran. Am J Sci 307: 1064-1095.

Allegre CO, Courtillot V, Tapponnier P, Hirn A, Mattauer M, Coulon C, Jaeger J, Achache J, Schärer U, Marcoux J (1984). Structure and evolution of the Himalaya–Tibet orogenic belt. Nature 307: 17-22.

Allen MB, Armstrong HA (2008). Arabia–Eurasia collision and the forcing of midCenozoic global cooling. Palaeogeogr Palaeoclimatol Palaeoecol 265: 52-58.

Almasi A (2016). Mineralization, petrogenesis and geochemical-geophysical exploration in Uch-Palang-Sarsefidal. PhD, Ferdowsi University of Mashhad, Mashhad, Iran.

Altherr R, Holl A, Hegner E, Langer C, Kreuzer H (2000). High-potassium, calc-alkaline I-type plutonism in the European Variscides: northern Vosges (France) and northern Schwarzwald (Germany). Lithos 50: 51-73.

Arjmandzadeh R, Karimpour MH, Mazaheri SA, Santos JF, Medina JM, Homam SM (2011). Sr-Nd isotope geochemistry and petrogenesis of the Chah-Shaljami granitoids, Lut Block, Eastern Iran. J Asian Earth Sci 41: 283-296.

Arjmandzadeh R, Santos JF (2014). Sr-Nd isotope geochemistry and tectonomagmatic setting of the Dehsalm Cu-Mo porphyry mineralizing intrusives from Lut Block, eastern Iran. Int J Earth Sci (Geol Rundsch) 103: 123-140.

Arslan M, Temizel İ, Abdioğlu E, Kolaylı H, Yücel C, Boztuğ D, Şen C (2013). ^{39}Ar-^{39}Ar dating, whole-rock and Sr-Nd-Pb isotope geochemistry of post-collisional Eocene volcanic rocks in the southern part of the Eastern Pontides (NE Turkey): implications for magma evolution in extension-induced origin. Contrib Mineral Petr 166: 113-142.

Asiabanha A, Foden J (2012). Post-collisional transition from an extensional volcanosedimentary basin to a continental arc in the Alborz Ranges, N-Iran. Lithos 148: 98-111.

Aslan Z, Arslan M, Temizel İ, Kaygusuz A (2014). K-Ar dating, whole-rock and Sr-Nd isotope geochemistry of calc-alkaline volcanic rocks around the Gümüşhane area: implications for post-collisional volcanism in the Eastern Pontides, Northeast Turkey. Miner Petrol 108: 245-267.

Aydınçakır E, Şen C (2013). Petrogenesis of the post-collisional volcanic rocks from the Borçka (Artvin) area: Implications for the evolution of the Eocene magmatism in the Eastern Pontides (NE Turkey). Lithos 172: 98-117.

Bagherzadeh RM, Karimpour MH, Farmer GL, Stern CR, Santos JF, Rahimi B, Heidarian Shahri MR (2015). U–Pb zircon geochronology, petrochemical and Sr–Nd isotopic characteristic of Late Neoproterozoic granitoid of the Bornaward Complex (Bardaskan, NE Iran). J Asian Earth Sci 111: 54-71.

Ballato P, Uba CE, Landgraf A, Strecker MR, Sudo M, Stockli DF, Friedrich A, Tabatabaei SH (2011). Arabia–Eurasia continental collision: insights from late Tertiary foreland-basin evolution in the Alborz Mountains, northern Iran. Geol Soc Am Bull 123: 106-131.

Barbarin B, Didier J (1992). Genesis and evolution of mafic microgranular enclaves through various types of interaction between coexisting felsic and mafic magmas. T Roy Soc Edin-Earth 83: 145-153.

Baroz F, Macaudiere J, Montigny R, Noghreyan M, Ohnenstetter M, Rocci G (1984). Ophiolites and related formations in the central part of the Sabzevar (Iran) and possible geotectonics reconstructions. Neu Jb Geol Paläont Abh 168: 358-388.

Behroozi A (1987). Geological Map of Feyzabad. Scale 1:100,000, Sheet 7760. Tehran, Iran: Geological Survey of Iran.

Berberian M, King GCP (1981). Towards a paleogeography and tectonic evolution of Iran. Can J Earth Sci 18: 210-265.

Bernhardt U (1983). Middle Tertiary Volcanic Rocks from the Southern Sabzevar Zone, Khorasan, NE Iran. Geodynamic Project (Geotraverse) in Iran, Geological Survey of Iran Report No. 51. Tehran, Iran: Geological Survey of Iran.

Bonin B (2004). Do coeval mafic and felsic magmas in post-collisional to within-plate regimes necessarily imply two contrasting, mantle and crustal, sources? A review. Lithos 78: 1-24.

Boztuğ D, Jonckheere RC, Wagner GA, Erçin Aİ, Yeğingil Z (2007). Titanite and zircon fission-track dating resolves successive igneous episodes in the formation of the composite Kaçkar batholith in the Turkish Eastern Pontides. Int J Earth Sci 96: 875-886.

Chappell BW, White AJR (1992). I- and S-type granites in the Lachlan Fold Belt. T Roy Soc Edin-Earth 83: 1-26.

Chen B, Jahn BM, Wei C (2002). Petrogenesis of Mesozoic granitoids in the Dabie UHP complex, Central China: trace element and Nd-Sr isotope evidence. Lithos 60: 67-88.

Cherniak DJ, Watson EB (2000). Pb diffusion in zircon. Chem Geol 172: 5-24.

Chiu HY, Chung SL, Zarrinkoub MH, Mohammadi SS, Khatib MM, Iizuka Y (2013). Zircon U–Pb age constraints from Iran on the magmatic evolution related to Neotethyan subduction and Zagros orogeny. Lithos 162-163: 70-87.

Davies JH, von Blanckenburg F (1995). Slab breakoff: a model of lithospheric detachment and its test in the magmatism and deformation of collisional orogens. Earth Planet Sci Lett 129: 85-102.

DePaolo DJ (1981). Trace-element and isotopic effects of combined wallrock assimilation and fractional crystallization. Earth Planet Sci Lett 53: 189-202.

DePaolo DJ, Wasserburg GJ (1979) Petrogenetic mixing models and Nd-Sr isotopic patterns. Geochim Cosmochim Ac 43: 615-627.

Dilek Y, Furnes H, Shallo M (2007). Suprasubduction zone ophiolite formation along the periphery of Mesozoic Gondwana. Gondwana Res 11: 453-475.

Dilek Y, Imamverdiyev N, Altunkaynak S (2010). Geochemistry and tectonics of Cenozoic volcanism in the Lesser Caucasus (Azerbaijan) and the peri-Arabian region: collision-induced mantle dynamics and its magmatic fingerprint. Int Geol Rev 52: 536-578.

Dokuz A (2011). A slab detachment and delamination model for the generation of Carboniferous high-potassium I-type magmatism in the eastern Pontides, NE Turkey: the Köse composite pluton. Gondwana Res 19: 926-944.

Eftekharnezhad J, Aghanabati A, Hamzehpour A (1974). Geological Map of Sabzevar, Scale 1:250000. Tehran, Iran: Geological Survey of Iran.

Ersoy EY, Cüneyt A, Can G, Osman C, Martin P, Dejan P, İbrahim U, Regina MK (2017). U-Pb zircon geochronology of the Paleogene – Neogene volcanism in the NW Anatolia: its implications for the Late Mesozoic-Cenozoic geodynamic evolution of the Aegean. Tectonophysics 717: 284-301.

Eyuboğlu Y, Chung SL, Dudas FO, Santosh M, Akaryali E (2011). Transition from shoshonitic to adakitic magmatism in the Eastern Pontides, NE Turkey: implications for slab window melting. Gondwana Res 19: 413-429.

Faure EG (1986). Principles of Isotope Geology. 2nd ed. New York, NY, USA: John Wiley and Sons.

Frost BR, Barnes CG, Collins WJ, Arculus RJ, Ellis DJ, Frost CD (2001). A geochemical classification for granitic rocks. J Petrol 41: 2033-2048.

Frost CD, Frost BR (2011). On ferroan (A-type) granitoids: their compositional variability and modes of origin. J Petrol 52: 39-53.

Gansser A (1981). The geodynamic history of the Himalaya, in Zagros, Hindu Kush. In: Gupta HK, Delany FM, editors. Himalaya-Geodynamic Evolution, Geodynamic Series 3. Washington, DC, USA: American Geophysical Union, pp. 111-121.

Göçmengil G, Karacık Z, Genç ŞC, Billor MZ (2018). ^{40}Ar-^{39}Ar geochronology and petrogenesis of postcollisional trachytic volcanism along the İzmir-Ankara-Erzincan Suture Zone (NE, Turkey). Turkish J Earth Sci 27: 1-31.

Golonka J, Bocharova NY (2000). Hot spot activity and the break-up of Pangea. Palaeogeogr Palaeocl 161: 49-69.

Green TH (1994). Experimental studies of trace element partitioning applicable to igneous petrogenesis-Sedona 16 years later. Chem Geol 117: 1-36.

Gülmez F, Genç SC, Keskin M, Tüysüz O (2013). A post-collision slab-breakoff model for the orgin of the Middle Eocene magmatic rocks of the Armutlu–Almacik belt, NW Turkey and its regional implications. Geol Soc Spec Publ 372: 107-139.

Hastie AR, Kerr AC, Pearce JA, Mitchell SF (2007). Classification of altered volcanic island arc rocks using immobile trace elements: development of the Th–Co discrimination diagram. J Petrol 48: 2341-2357.

Henderson P (1984). General geochemical properties and abundances of the rare earth elements. In: Henderson P, editor. Rare Earth Element Geochemistry. Amsterdam, the Netherlands: Elsevier, pp. 1-32.

Hildreth W (1981). Gradients in silicic magma chambers: implications for lithospheric magmatism. J Geophys Res 86: 153-192.

Hou ZQ, Cook NJ (2009). Metallogenesis of the Tibetan Collisional Orogen: a review and introduction to the special issue. Ore Geol Rev 36: 2-24.

Huang XL, Xu YG, Li XH, Li WX, Lan JB, Zhang HH, Liu YS, Wang YB, Li HY, Luo ZY et al. (2008). Petrogenesis and tectonic implications of Neoproterozoic, highly fractionated A-type granites from Mianning, South China. Precambr Res 165: 190-204.

Jahn BR (2004). The central Asian orogenic belt and growth of the continental crust in the Phanerozoic. In: Malpas J, Fletcher CJN, Ali JR, Aitchison JC, editors. Aspects of the Tectonic Evolution of China. London, UK: Geological Society of London, pp. 73-100.

Jiang XY, Li XH (2014) In situ zircon U–Pb and Hf–O isotopic results for ca. 73 Ma granite in Hainan Island: implications for the termination of an Andean-type active continental margin in southeast China. J Asian Earth Sci 82: 32-46.

Karimpour MH (2004). Mineralogy, alteration, source rock, and tectonic setting of iron-oxides Cu–Au deposits and examples of Iran. In: 11th Iranian Crystallography and Mineralogy Society of Iran Proceedings, pp. 184-189.

Karsli O, Dokuz A, Uysal Aydin F, Chen B, Kandemir R, Wijbrans J (2010). Relative contributions of crust and mantle to generation of Campanian high-K calc-alkaline I-type granitoids in a subduction setting, with special reference to the Harşit Pluton, Eastern Turkey. Contrib Mineral Petr 167: 467-487.

Kasapoğlu B, Ersoy YE, Uysal İ, Palmer MR, Zack T, Koralay EO, Karlsson A (2016). The petrology of Paleogene volcanism in the Central Sakarya, Nallıhan Region: implications for the initiation and evolution of post-collisional, slab break-off related Magmatic activity. Lithos 246: 81-98.

Kaygusuz A (2011). Calc-alkaline I-type plutons in the eastern Pontides, NE Turkey: U–Pb zircon ages, geochemical and Sr–Nd isotopic compositions. Chem Erde Geochem 71: 59-75.

Kaygusuz A, Arslan M, Siebel W, Sipahi F, İlbeyli N, Temizel İ (2014). LA-ICP MS zircon dating, whole-rock and Sr–Nd–Pb–O isotope geochemistry of the Camiboğazı pluton, Eastern Pontides, NE Turkey: implications for lithospheric mantle and lower crustal sources in arc-related I-type magmatism. Lithos 192: 271-290.

Kaygusuz A, Siebel W, Sen C, Satir M (2008). Petrochemistry and petrology of I-type granitoids in an arc setting: the composite Torul pluton, Eastern Pontides, NE Turkey. Int J Earth Sci 97: 739-764.

Kemp AIS, Hawkesworth CJ, Collins WJ, Gray CM, Blevin PL, Eimf (2009). Isotopic evidence for rapid continental growth in an extensional accretionary orogen: the Tasmanides, eastern Australia. Earth Planet Sc Lett 284: 455-466.

Keskin M, Genç SC, Tüysüz O (2008). Petrology and geochemistry of post-collisional Middle Eocene volcanic units in North-Central Turkey: evidence for magma generation by slab breakoff following the closure of the Northern Neotethys Ocean. Lithos 104: 267-305.

Kinzler RJ (1997). Melting of mantle peridotite at pressure approaching the spinel to garnet transition: application to mid ocean ridge petrogenesis. J Geophys Res 102: 853-874.

Klein EM (2004). Geochemistry of the igneous oceanic crust. In: Holland HD, Turekian KK, editors. Treatise on Geochemistry. Amsterdam, the Netherlands: Elsevier, pp. 433-463.

Koop W, Stoneley R, Ridd M, Murphy R, Osmaston M, Kholief M (1982). Subsidence history of the Middle East Zagros basin, Permian to Recent [and discussion]. Philos Trans R Soc Lond Ser A Math Phys Sci 305: 149-168.

Lambert RJ, Holland JG (1974). Yttrium geochemistry applied to petrogenesis utilizing calcium–yttrium relationships in minerals and rocks. Geochim Cosmochim Ac 38: 1393-1414.

Langmuir CH, Vocke RD, Hanson GN, Hart SR (1978). A general mixing equation with applications to Icelandic basalts. Earth Planet Sc Lett 37: 380-392.

Li X (2013). Alkaline magmatism, water-rock interaction and multiple metamorphism in the Seiland Igneous Province, Northern Norway. PhD, Albert Ludwig University of Freiburg, Freiburg, Germany.

Malekzadeh Shafaroudi A, Karimpour MH, Golmohammadi A (2013). Zircon U–Pb geochronology and petrology of intrusive rocks in the C-North and Baghak districts, Sangan iron mine, NE Iran. J Asian Earth Sci 64: 256-271.

Martin H (1994). The Archean grey gneisses and the genesis of the continental crust. Developments in Precambrian Geology 11: 205-259.

Martin H (1999). The adakitic magmas: modern analogues of Archaean granitoids. Lithos 46: 411-429.

McDougall I, Harrison TM (1988). Geochronology and Thermochronology by the $^{40}Ar/^{39}Ar$ Method. Oxford, UK: Oxford University Press.

McKenzie D, O'Nions RK (1991). Partial melt distributions from inversion of rare earth element concentrations. J Petrol 32: 1021-1091.

McQuarrie N, Stock, JM, Verdel, C and Wernicke BP (2003). Cenozoic evolution of Neotethys and implications for the causes of plate motions. Geophys Res Lett 30: 2036.

Middlemost EAK (1985). Naming materials in the magma/igneous rock system. Earth-Sci Rev 37: 215-224.

Moix P, Beccaletto L, Kozur HW, Hochard C, Rosselet F, Stampfli GM (2008). A new classification of the Turkish terranes and sutures and its implication for the paleotectonic history of the region. Tectonophysics 451: 7-39.

Mouthereau F, Lacombe O, Vergés J (2012). Building the Zagros collisional orogen: timing, strain distribution and the dynamics of Arabia/Eurasia plate convergence. Tectonophysics 532: 27-60.

Naderi Mighan N, Torshizian H (1999). Geological Map of Kadkan, Scale 1:100000. Tehran, Iran: Geological Survey of Iran.

Omrani J, Agard P, Whitechurch H, Benoit M, Prouteau G, Jolivet L (2008). Arc magmatism and subduction history beneath the Zagros Mountains, Iran: a new report of adakites and geodynamic consequences. Lithos 106: 380-398.

Pang KN, Chung SL, Zarrinkoub MH, Khatib MM, Mohammadi SS, Chiu HY, Chu CH, Lee HY, Lo CH (2013). Eocene–Oligocene post-collisional magmatism in the Lut–Sistan region, eastern Iran: magma genesis and tectonic implications. Lithos 180-181: 234-251.

Pearce JA (1996). Sources and settings of granitoids rocks. Episodes 19: 120-125.

Pearce JA, Bender JF, De Long SE, Kidd WSF, Low PJ, Güner Y, Saroglu F, Yilmaz Y, Moorbath S, Mitchell JG (1990). Genesis of collision volcanism in Eastern Anatolia, Turkey. J Volcanol Geoth Res 44: 189–229.

Pearce JA, Harris NBW, Tindle AG (1984). Trace element discrimination diagrams for the tectonic interpretation of granitic rocks. J Petrol 25: 956-983.

Pearce JA, Parkinson IJ (1993). Trace element models for mantle melting: application to volcanic arc petrogenesis. In: Prichard HM, Albaster T, Harris NBW, Neary CR, editors. Magmatic Processes in Plate Tectonics. London, UK: Geological Society of London, pp. 373-403.

Peccerillo A, Taylor SR (1976). Geochemistry of Eocene calc-alkaline volcanic rocks from the Kastamonu area, northern Turkey. Contrib Miner Petrol 58: 63-81.

Perugini D, Poli G (2004). Analysis and numerical simulation of chaotic advection and chemical diffusion during magma mixing: petrological implications. Lithos 78: 43-66.

Ramezani J, Tucker RD (2003). The Saghand Region, Central Iran: U–Pb geochronology, petrogenesis and implications for Gondwana Tectonics. Am J Sci 303: 622-665.

Ramsey LA, Walker RT, Jackson J (2008). Fold evolution and drainage development in the Zagros Mountains of Fars province, SE Iran. Basin Res 20: 23-48.

Rapp PR, Shimizu N, Norman MD (1999). Applegate, reaction between slab-derived melt and peridotite in the mantle wedge: experimental constrains at 3.8 Gpa. Chem Geol 160: 335-356.

Reagan MK, Gill JB (1989). Coexisting calc-alkaline and high niobium basalts from Turrialba volcano, Costa Rica: implication for residual titanates in arc magma source. J Geophys Res 94: 4619-4633.

Rubatto D (2002). Zircon trace element geochemistry: partitioning with garnet and the link between U-Pb ages and metamorphism. Chem Geol 184: 123-138.

Rubatto D, Williams IS, Buick IS (2001). Zircon and monazite response to prograde metamorphism in the Reynolds Range Central Australia. Contrib Mineral Petr 140: 458-468.

Sahandi MR, Hoseini M (1990). Geological Map of Sabzevar, Scale 1:100000. Tehran, Iran: Geological Survey of Iran.

Samiee S, Karimpour MH, Ghaderi M, Haidarian Shahri MR, Klöetzli U, Santos JF (2016). Petrogenesis of subvolcanic rocks from the Khunik prospecting area, south of Birjand, Iran: geochemical, Sr–Nd isotopic and U–Pb zircon constraints. J Asian Earth Sci 115: 170-182.

Şengör AMC (1987). Tectonics of the Tethysides: orogenic collage development in a collisional setting. Annu Rev Earth Planet Sci 15: 213-244.

Şengör AMC (1990). A new model for the late Palaeozoic—Mesozoic tectonic evolution of Iran and implications for Oman. Geol Soc Spec Publ 49: 797-831.

Sengör AMC, Natalin BA (1996). Palaeotectonics of Asia: fragments of a synthesis. In: Yin A, Harrison M, editors. The Tectonic Evolution of Asia. Cambridge, UK: Cambridge University Press, pp. 443-486.

Şengör AMC, Yilmaz Y (1981). Tethyan evolution of Turkey: a plate tectonic approach. Tectonophysics 75: 181-241.

Shafaii Moghadam HS, Corfu F, Chiaradia M, Stern RJ, Ghorbani G (2014). Sabzevar Ophiolite, NE Iran: progress from embryonic oceanic lithosphere into magmatic arc constrained by new isotopic and geochemical data. Lithos 210-211: 224-241.

Shafaii Moghadam HS, Li XH, Ling XX, Santos JF, Stern RJ, Li QL, Ghorbani G (2015). Eocene Kashmar granitoids (NE Iran): petrogenetic constraints from U–Pb zircon geochronology and isotope geochemistry. Lithos 216-217: 118-135.

Shafaii Moghadam HS, Li XH, Stern RJ, Ghorbani G, Bakhshizad F (2016). Zircon U-Pb ages and Hf-O isotopic composition of migmatites from the Zanjan-Takab complex, NW Iran: constraints on partial melting of metasediments. Lithos 240: 34-48.

Shafiei B, Haschke M, Shahabpour J (2009). Recycling of orogenic arc crust triggers porphyry Cu mineralization in Kerman Cenozoic arc rocks, southeastern Iran. Miner Deposita 44: 265-283.

Shahabpour J (2005). Tectonic evolution of the orogenic belt in the region located between Kerman and Neyriz. J Asian Earth Sci 24: 405-417.

Shand SJ (1943). Eruptive Rocks. London, UK: T. Murby.

Sisson TW, Grove TL (1993). Experimental investigations of the role of H_2O in calc-alkaline differentiation and subduction zone magmatism. Contrib Mineral Petr 113: 143-166.

Soltani A (2000). Geochemistry and Geochronology of I-Type Granitoid Rocks in the Northeastern Central Iran Plate. Wollongong, Australia: University of Wollongong.

Stampfli GM, Borel GD (2002). A plate tectonic model for the Paleozoic and Mesozoic constrained by dynamic plate boundaries and restored synthetic oceanic isochrons. Earth Planet Sci Lett 196: 17-33.

Stöcklin J (1968). Structural history and tectonics of Iran, a review. Am Assoc Pet Geol Bull 52: 229-1258.

Sun SS, McDonough WF (1989). Chemical and isotopic systematic of oceanic basalts: implications for mantle composition and processes. Geol Soc Lond 42: 313-345.

Sun W, Williams I, Li S (2002). Carboniferous and Triassic eclogites in the western Dabie Mountains, east-central China: evidence for protracted convergence of the North and South China blocks. J Metamorph Geol 20: 873-886.

Taylor SR, McLennan SM (2009). Planetary Crusts: Their Composition, Origin and Evolution. Cambridge, UK: Cambridge University Press.

Temizel İ, Arslan M, Ruffet G, Peucat JJ (2012). Petrochemistry, geochronology and Sr-Nd isotopic systematics of the Tertiary collisional and post-collisional volcanic rocks from the Ulubey (Ordu) area, eastern Pontide, NE Turkey: implications for extension-related origin and mantle source characteristics. Lithos 128: 126-147.

Temizel I, Arslan M, Yücel C, Abdioğlu E, Ruffet G (2016). Geochronology and geochemistry of Eocene-aged volcanic rocks around the Bafra (Samsun, N Turkey) area: constraints for the interaction of lithospheric mantle and crustal melts. Lithos 258: 92-114.

Topuz G, Alther R, Schwarz WH, Siebel W, Satır M, Dokuz A (2005). Post-collisional plutonism with adakite-like signatures: the Eocene Saraycık granodiorite (eastern Pontides, Turkey). Contrib Mineral Petr 150: 441-455.

Vaezipour MJ, Alavi Tehrani MJ, Behroozi A (1993). Geological map of Torbat e Heydariyeh, Scale 1:250000. Tehran, Iran: Geological Survey of Iran.

Verdel C, Wernicke BP, Hassanzadeh J, Guest B (2011). A Paleogene extensional arc flare-up in Iran. Tectonics 30: TC3008.

Verdel C, Wernicke BP, Ramezani J, Hassanzadeh J, Renne PR, Spell TL (2007). Geology and thermochronology of Tertiary Cordilleran-style metamorphic core complexes in the Saghand region of central Iran. Geol Soc Am Bull 119: 961-977.

Vincent SJ, Allen MB, Ismail-Zadeh AD, Flecker R, Foland KA, Simmons MD (2005). Insights from the Talysh of Azerbaijan into the Paleogene evolution of the South Caspian region. Geol Soc Am Bull 117: 1513-1533.

Walker R, Jackson J (2004). Active tectonics and late Cenozoic strain distribution in central and eastern Iran. Tectonics 23: TC5010.

Walter MJ (1998). Melting of garnet peridotite and the origin of komatiite and depleted lithosphere. J Petrol 39: 29-60.

Wang XX, Wang T, Happala I, Lu XX (2002). Genesis of mafic enclaves from rapakivi-textured granites in the Qinling and its petrological significance: evidence of elements and Nd, Sr isotopes. Acta Petrologica Sinica 21: 935-946 (in Chinese with English abstract).

White AJR, Chappell BW (1983). Granitoid types and their distribution in the Lachlan Fold Belt, southeastern Australia. Geol Soc Am Memoir 159: 2l-34.

Williams IS (2001). Response of detrital zircon and monazite, and their U-Pb isotopic systems, to regional metamorphism and host-rock partial melting, Cooma Complex, southeastern Australia. Aust J Earth Sci 48: 557-580.

Wu Y, Zheng Y (2004). Genesis of zircon and its constraints on interpretation of U-Pb age. Chin Sci Bull 49: 1554-1569.

Yücel C, Arslan M, Temizel İ, Yazar EA, Ruffet G (2017). Evolution of K-rich magmas derived from a net veined lithospheric mantle in an ongoing extensional setting: Geochronology and geochemistry of Eocene and Miocene volcanic rocks from Eastern Pontides (Turkey). Gondwana Res 45: 65-86.

Zhong H, Zhu WG, Hu RZ, Xie LW, He DF, Liu F, Chu ZY (2009). Zircon U–Pb age and Sr–Nd–Hf isotope geochemistry of the Panzhihua A-type syenitic intrusion in the Emeishan large igneous province, southwest China and implications for growth of juvenile crust. Lithos 110: 109-128.

Zindler A, Hart SR (1986). Chemical geodynamics. Annu Rev Earth Planet Sci 14: 493-571.